COMMUN. MATH. SCI.
Vol. 17, No. 3, pp. 835–858

NUMERICAL APPROXIMATIONS FOR THE HYDRODYNAMICS COUPLED BINARY SURFACTANT PHASE FIELD MODEL: SECOND-ORDER, LINEAR, UNCONDITIONALLY ENERGY STABLE SCHEMES*

CHEN XU†, CHUANJUN CHEN‡, XIAOFENG YANG§, AND XIAOMING HE¶

Abstract. In this paper, we consider numerical approximations of a binary fluid-surfactant phase-field model coupled with the fluid flow, in which the system consists of the incompressible Navier-Stokes equations and two Cahn-Hilliard type equations. We develop two linear and second order time marching schemes for solving this system by combining the "Invariant Energy Quadratization" approach for the nonlinear potentials, the projection method for the Navier-Stokes equation, and a subtle implicit-explicit treatment for the stress and convective terms. We prove the well-posedness of the linear system and its unconditional energy stability rigorously. Various 2D and 3D numerical experiments are performed to validate the accuracy and energy stability of the proposed schemes.

Keywords. Phase-field; fluid-surfactant; Navier-Stokes; Cahn-Hilliard; Second order; Energy stability.

AMS subject classifications. 60F10; 60J75; 62P10; 92C37.

1. Introduction

In this paper, we consider numerical approximations of a hydrodynamics coupled binary fluid-surfactant phase-field model. The governing system consists of incompressible Navier-Stokes equations and two Cahn-Hilliard type equations. Surfactants are compounds that can alter the surface tension (or interfacial tension) between two liquids, between a gas and a liquid, or between a liquid and a solid. They may act as detergents, wetting agents, emulsifiers, foaming agents, and dispersants. In the modeling and numerical simulations for investigating the binary fluid-surfactant system, the phase field method had been widely used to study the phase transition behaviors of the monolayer microemulsion system formed by soluble surfactant moleculses, see the pioneering modeling work of Laradji et. al. in [25, 26] where the first surfactant phase field model was developed, and a number of subsequent modeling/simulation advances in [2, 9, 24, 42, 43].

While numerous fluid surfactant phase models had been given attentions for more than twenty years, a non-negligible fact is, almost all developed numerical algorithms had been focused on the *partial* model, i.e., no flow field had been considered, which implies that the inherent numerical challenges are greatly diminished. For the partial model, one only needs to consider how to discretize the nonlinear stiff terms, for instance, the cubic term induced by the double-well potential, or the term induced by the logarithmic Flory-Huggins potential. To name a few, in [23], a second order in

*Received: May 9, 2018; Accepted (in revised form): February 21, 2019. Communicated by John Lowengrub.

†Institute of Intelligent Computing Science, Shenzhen University, Shenzhen 518060, P.R. China (xuchen@szu.edu.cn).

‡Corresponding author. School of Mathematics and Information Sciences, Yantai University, Yantai 264005, China (cjchen@ytu.edu.cn).

§Department of Mathematics, University of South Carolina, Columbia, SC 29208, USA (xfyang@math.sc.edu).

¶Department of Mathematics and Statistics, Missouri University of Science and Technology, Rolla, MO 65409, USA; School of Mathematical Sciences, University of Electronic Science and Technology of China, Chengdu, 610054, China (hex@mst.edu).

time, nonlinear scheme was developed based on the Crank-Nicolson method to solve the partial model, however, the scheme is not provably energy stable. In [13], the authors developed a first order in time, nonlinear scheme based on the convex splitting approach, where the convex part of the free energy potential is treated implicitly while the concave part is treated explicitly, but the arguments about the convex-concave decomposition for the coupling potential are not valid as well since it is not sufficient to justify the convexity of a function with multiple variables from the positivity of second-order partial derivatives. In [57], the authors developed two provably, unconditionally energy stable, linear and second order schemes. But the model considered in [57] is still the partial model without considering the flow filed.

Compared with the partial model without flow fields, in addition to the stiffness issue mentioned above, the full hydrodynamical surfactant model is conceivably more complicated for algorithms design since one must consider developing efficient temporal discretizations for the nonlinear coupling terms between the flow field and phase field variables through stress and convective terms. Simple fully-implicit or explicit type discretizations for those terms will induce unfavorable nonlinear and/or energy unstable schemes, so they are not efficient in practice. Therefore, in this paper, the main purpose is to develop unconditionally energy stable schemes for solving the full hydrodynamics coupled fluid-surfactant model. Specifically, we choose the model developed in [9, 42] since it is not only a typical representative of nonlinearly coupled multivariate fluid-surfactant models, but also *mathematically reasonable*, i.e., the total energy is naturally bounded from below. By combining some well-known approaches like the projection method for Navier-Stokes equations, the Invariant Energy Quadratizaiton (IEQ) approach for nonlinear stiff terms, and implicit-explicit treatments for nonlinear stresses, we obtain two linear, second order, and provably unconditionally energy stable time marching schemes. Moreover, we rigorously prove that the well-posedness and unconditional energy stabilities hold, and demonstrate the stability and the accuracy of the proposed schemes through a number of classical benchmark phase separation simulations. To the best of the authors' knowledge, the proposed schemes here are the first linear schemes with second-order temporal accuracy for the hydrodynamics coupled phase field surfactant model with provable unconditional energy stabilities.

The rest of the paper is organized as follows. In Section 2, we introduce the binary fluid-surfactant phase field model developed in [9, 42] and reformulate it to couple the Navier-Stokes equations. In Section 3, we present two, second order numerical schemes for simulating the target model, and rigorously prove that the produced linear systems are well-posed and the schemes satisfy the unconditional energy stabilities. Various 2D and 3D numerical experiments are carried out in Section 4 to verify the accuracy and stability of these schemes. Finally, some concluding remarks are given in Section 5.

2. The flow coupled surfactant model and its energy law

We fix some notations first. We consider an open, bounded, connected domain $\Omega \in \mathbb{R}^d, d = 2,3$ with $\partial\Omega$ Lipschitz continuous. For any $f(\boldsymbol{x}), g(\boldsymbol{x}) \in L^2(\Omega)$, we denote the inner product and L^2 norm as

$$(f,g) = \int_\Omega f(\boldsymbol{x}) g(\boldsymbol{x}) d\boldsymbol{x}, \quad \|f\| = \int_\Omega |f(\boldsymbol{x})|^2 d\boldsymbol{x}. \tag{2.1}$$

Let $W^{k,r}(\Omega)$ stands for the standard Sobolev spaces equipped with the standard Sobolev norms $\|\cdot\|_{k,r}$. For $r = 1$, we write $H^1(\Omega)$ for $W^{1,2}(\Omega)$ and its corresponding norm is $\|\cdot\|_{H^1}$.

We now give a brief description for the total free energy for the fluid-surfactant phase

field model that was developed in [9,42]. In the binary fluid-surfactant system, monolayers of surfactant molecules form microemulsions as a random phase. The phase field modeling approach simulates the dynamics of microphase separation in microemulsion systems using two phase field variables (order parameters). In the phase field framework, a phase field variable $\phi(\boldsymbol{x},t)$ is introduced to represent the local densities of the two fluids, fluid I and fluid II (such as water and oil), such that

$$\phi(\boldsymbol{x},t)=\begin{cases}-1 & \text{fluid I},\\ 1 & \text{fluid II},\end{cases} \tag{2.2}$$

with a thin smooth transition layer of width $O(\epsilon)$ connecting the two fluids. Thus the interface of the mixture is described by the zero level set $\Gamma_t=\{\boldsymbol{x}:\phi(\boldsymbol{x},t)=0\}$. In the fluid-surfactant model, an extra phase field variable $\rho(\boldsymbol{x},t)$ is needed to represent the local concentration of surfactants. Furthermore, we use ϱ and $\boldsymbol{u}$ to represent the volume-averaged density of the mixture system and volume-averaged velocity field, respectively. Thus, after coupling with the hydrodynamics, the total energy of the binary mixture fluid-surfactant system is the sum of the kinetic energy $\boldsymbol{E}_k(\varrho,\boldsymbol{u})$, the mixing energy $\boldsymbol{E}_1(\phi)$, the logarithmic energy $\boldsymbol{E}_2(\rho)$, and the coupling entropy term $\boldsymbol{E}_3(\rho,\phi)$, given as follows,

$$\begin{aligned}\boldsymbol{E}_{tot}(\boldsymbol{u},\phi,\rho)=&\underbrace{\int_\Omega\Big(\frac{\epsilon}{2}|\nabla\phi|^2+\frac{1}{4\epsilon}F(\phi)\Big)d\boldsymbol{x}}_{\boldsymbol{E}_1(\phi)}+\underbrace{\int_\Omega\Big(\frac{\eta}{2}|\nabla\rho|^2+\beta G(\rho)\Big)d\boldsymbol{x}}_{\boldsymbol{E}_2(\rho)}\\&+\underbrace{\frac{\alpha}{2}\int_\Omega(\rho-|\nabla\phi|^2)d\boldsymbol{x}}_{\boldsymbol{E}_3(\rho,\phi)}+\underbrace{\int_\Omega\frac{1}{2}\varrho|\boldsymbol{u}|^2d\boldsymbol{x}}_{\boldsymbol{E}_k(\varrho,\boldsymbol{u})},\end{aligned} \tag{2.3}$$

where $\epsilon,\eta,\alpha,\beta$ are all positive parameters.

We describe these energy components as follows. First, $\boldsymbol{E}_1(\phi)$ is the mixing free energy functional and $F(\phi)$ is the classical double-well potential which is defined as

$$F(\phi)=(\phi^2-1)^2. \tag{2.4}$$

In fact, $\boldsymbol{E}_1(\phi)$ is the most commonly used free energy in phase field models so far, where the first term in $\boldsymbol{E}_1(\phi)$ contributes to the hydrophilic type (tendency of mixing) of interactions between the materials and the second term represents the hydrophobic type (tendency of separation) of interactions. As a consequence of the competition between the two types of interactions, the equilibrium configuration will include a diffusive interface. The phase field models that are derived by this part of free energy have been extensively studied, see [1,17,21,27] and the references therein.

Second, in the free energy $\boldsymbol{E}_2(\rho)$, the gradient potential $|\nabla\rho|^2$ is added in order to enhance the stability, and the nonlinear potential $G(\rho)$ is defined as

$$G(\rho)=\rho\ln\rho+(1-\rho)\ln(1-\rho), \tag{2.5}$$

where β and η (both are in the same scale as ϵ) are two positive parameters. We note that $G(\rho)$ is the logarithmic Flory-Huggins-type energy potential which restricts the value of ρ to be inside the domain of $(0,1)$, and ρ will reach its upper bound if the interface is fully saturated with surfactant, see [43].

Third, the free energy $\boldsymbol{E}_3(\phi,\rho)$ couples the two variables ϕ and ρ, which is the penalty term that enables the concentration to accumulate near the interface with a relatively high value.

In this paper, we only consider the case where the two fluid components have matching density and viscosity, i.e., $\varrho_1=\varrho_2=1$ and $\nu_1=\nu_2=\nu$ for simplicity. Following the generalized Onsager's principle [29], we derive the following governing system of equations and present them in dimensionless forms:

$$\boldsymbol{u}_t+(\boldsymbol{u}\cdot\nabla)\boldsymbol{u}+\nabla p-\nu\Delta\boldsymbol{u}+\phi\nabla\mu_\phi+\rho\nabla\mu_\rho=0, \tag{2.6}$$

$$\nabla\cdot\boldsymbol{u}=0, \tag{2.7}$$

$$\phi_t+\nabla\cdot(\boldsymbol{u}\phi)=M_1\Delta\mu_\phi, \tag{2.8}$$

$$\mu_\phi=-\epsilon\Delta\phi+\frac{1}{\epsilon}\phi(\phi^2-1)+\alpha\nabla\cdot\Big((\rho-|\nabla\phi|)\boldsymbol{Z}\Big), \tag{2.9}$$

$$\rho_t+\nabla\cdot(\boldsymbol{u}\rho)=M_2\Delta\mu_\rho, \tag{2.10}$$

$$\mu_\rho=-\eta\Delta\rho+\alpha(\rho-|\nabla\phi|)+\beta\ln\Big(\frac{\rho}{1-\rho}\Big), \tag{2.11}$$

where $\boldsymbol{Z}(\phi)=\frac{\nabla\phi}{|\nabla\phi|}$, M_1 and M_2 are two mobility parameters. For simplicity, we take the periodic boundary conditions to remove all complexities from the boundary integrals.

The above system (2.6)-(2.11) follows the energy dissipation law. To do so, by taking the L^2 inner products of (2.6) with $\boldsymbol{u}$, of (2.8) with μ_ϕ, of (2.9) with $-\phi_t$, of (2.10) with μ_ρ, and of (2.11) with $-\rho_t$, using integration by parts, and combining all equalities, we obtain

$$\frac{d}{dt}\boldsymbol{E}_{tot}(\boldsymbol{u},\phi,\rho)=-\nu\|\nabla\boldsymbol{u}\|^2-M_1\|\nabla\mu_\phi\|^2-M_2\|\nabla\mu_\rho\|^2\le 0. \tag{2.12}$$

In the sequel, our goal is to design temporal approximation schemes which satisfy the discrete version of the continuous energy law (2.12).

Remark 2.1. For comparisons, we list the total free energy for the phase field model developed by Laradji et. al. in [24–26], that is

$$\begin{aligned}E(\phi,\rho)=&\int_\Omega\Big(\frac{\alpha}{2}(\Delta\phi)^2+\frac{\epsilon}{2}|\nabla\phi|^2+\frac{1}{4\epsilon}F(\phi)\Big)d\boldsymbol{x}+\int_\Omega\Big(\frac{\beta}{2}|\nabla\rho|^2+\frac{1}{4\eta}\rho^2(\rho-\rho_s)^2\Big)d\boldsymbol{x}\\&-\int_\Omega\theta\rho|\nabla\phi|^2d\boldsymbol{x}\end{aligned} \tag{2.13}$$

We note that there are some substantial differences between (2.13) and (2.3). The first difference is that the double-well-type potential is used for the concentration variable ρ in (2.13), instead of the logarithmic potential used in (2.3). The second one is that the format of the coupling free energy (associated with θ) are quite different. It is remarkable that this coupling term in (2.13) actually brings up significant challenges to prove the total free energy (2.13) to be bounded from below, see the detailed discussions in [8].

3. Numerical schemes

We next construct schemes for discretizing the flow coupled surfactant model (2.6)-(2.11) in time. To this end, there is a number of numerical challenges, including (i) how to discretize the cubic term associated with the double-well potential (see the related extensive studies in [4, 10, 20, 36, 48, 59, 61]); (ii) how to discretize the logarithmic term induced by the Flory-Huggins potential; (iii) how to discretize the local coupling entropy terms associated with ρ and ϕ; (iv) how to solve the Navier-Stokes equations; and (v) how to discretize the nonlinear convective and stress terms.

For (i), (ii) and (iii), we adopt the recently developed IEQ approach (cf. [18, 54–57, 60, 61, 63, 64]) to design desired numerical schemes. The intrinsic idea of the IEQ method is to transform the nonlinear potential into quadratic forms in terms of some new variables. This method is workable since we notice that all nonlinear potentials in the free energy are bounded from below. For (iv), we use the second order pressure correction method [15], where the pressure is then decoupled from the computations of the velocity. For (v), we use a subtle implicit-explicit treatment to obtain the fully linear schemes.

Since the numerical scheme can hardly guarantee that the numerical solution ρ is located in its domain (0,1), here we follow the work in [5, 7] to regularize the Flory-Huggins potential from domain (0,1) to $(-\infty,\infty)$. The idea is to replace the logarithmic functional by a C^2 continuous, convex and piece-wisely defined function. Namely, for any $\widehat{\epsilon}>0$, the regularized Flory-Huggins potential is given by

$$\widehat{G}(\rho)=\begin{cases}\rho\ln\rho+\frac{(1-\rho)^2}{2\widehat{\epsilon}}+(1-\rho)\ln\widehat{\epsilon}-\frac{\widehat{\epsilon}}{2}, & \text{if} \quad \rho\geq 1-\widehat{\epsilon},\\ \rho\ln\rho+(1-\rho)\ln(1-\rho), & \text{if} \quad \widehat{\epsilon}\leq\rho\leq 1-\widehat{\epsilon},\\ (1-\rho)\ln(1-\rho)+\frac{\rho^2}{2\widehat{\epsilon}}+\rho\ln\widehat{\epsilon}-\frac{\widehat{\epsilon}}{2}, & \text{if} \quad \rho\leq\widehat{\epsilon}.\end{cases} \tag{3.1}$$

When $\widehat{\epsilon}\to 0$, $\widehat{G}(\rho)\to G(\rho)$. Thus we consider the numerical solution to the model formulated with the regularized functional $\widehat{G}(\rho)$, but omit the $\widehat{\ }$ in the notation for convenience. For the Cahn-Hilliard equation, it has been proved that the error bound between the regularized system and the original system is controlled by $\widehat{\epsilon}$ up to a constant scaling, see [5, 7].

Note that $G(\rho)$ is actually bounded from below even though it is not always positive in the whole domain, thus we can rewrite the free energy functional in the following equivalent form:

$$\begin{aligned}\boldsymbol{E}_{tot}(\boldsymbol{u},\phi,\rho)=\int_\Omega\Big(&\frac{1}{2}|\boldsymbol{u}|^2+\frac{\epsilon}{2}|\nabla\phi|^2+\frac{\eta}{2}|\nabla\rho|^2+\frac{1}{4\epsilon}(\phi^2-1)^2\\&+\frac{\alpha}{2}(\rho-|\nabla\phi|)^2+\beta(\sqrt{G(\rho)+A}\,)^2\Big)d\boldsymbol{x}-\beta A|\Omega|,\end{aligned} \tag{3.2}$$

where A is a positive constant to ensure $G(\rho)+A>0$ (in all numerical examples, we use $A=1$). Note the free energy is still the same because we simply add a zero term $\beta A-\beta A$ to the energy density functional. Then we define three auxiliary variables to be the square root of the nonlinear potentials $F(\phi)$, $(\rho-|\nabla\phi|)^2$ and $G(\rho)+A$ by

$$U=\phi^2-1, \tag{3.3}$$

$$V=\rho-|\nabla\phi|, \tag{3.4}$$

$$W=\sqrt{G(\rho)+A}. \tag{3.5}$$

In turn, the total free energy (3.2) can be transformed as

$$\begin{aligned}\boldsymbol{E}_{tot}(\boldsymbol{u},\phi,\rho,U,V,W)=\int_\Omega\Big(&\frac{1}{2}|\boldsymbol{u}|^2+\frac{\epsilon}{2}|\nabla\phi|^2+\frac{\eta}{2}|\nabla\rho|^2+\frac{1}{4\epsilon}U^2+\frac{\alpha}{2}V^2+\beta W^2\Big)d\boldsymbol{x}\\&-\beta A|\Omega|.\end{aligned} \tag{3.6}$$

Then we obtain a new, but equivalent partial differential system as follows:

$$\boldsymbol{u}_t+(\boldsymbol{u}\cdot\nabla)\boldsymbol{u}+\nabla p-\nu\Delta\boldsymbol{u}+\phi\nabla\mu_\phi+\rho\nabla\mu_\rho=0, \tag{3.7}$$

$$\nabla\cdot\boldsymbol{u}=0, \tag{3.8}$$
$$\phi_t+\nabla\cdot(\phi\boldsymbol{u})=M_1\Delta\mu_\phi, \tag{3.9}$$
$$\mu_\phi=-\epsilon\Delta\phi+\frac{1}{\epsilon}\phi U+\alpha\nabla\cdot(V\boldsymbol{Z}), \tag{3.10}$$
$$\rho_t+\nabla\cdot(\rho\boldsymbol{u})=M_2\Delta\mu_\rho, \tag{3.11}$$
$$\mu_\rho=-\eta\Delta\rho+\alpha V+\beta H(\rho)W, \tag{3.12}$$
$$U_t=2\phi\phi_t, \tag{3.13}$$
$$V_t=\rho_t-\boldsymbol{Z}\cdot\nabla\phi_t, \tag{3.14}$$
$$W_t=\frac{1}{2}H(\rho)\rho_t, \tag{3.15}$$

with $H(\rho)=\frac{g(\rho)}{\sqrt{G(\rho)+A}}$ where $g(\rho)=G'(\rho)$.

The initial conditions are correspondingly

$$\begin{cases}\boldsymbol{u}|_{(t=0)}=\boldsymbol{u}_0,\ \phi|_{(t=0)}=\phi_0,\ \rho|_{(t=0)}=\rho_0,\\ U|_{(t=0)}=\phi_0^2-1,\ V|_{(t=0)}=\rho_0-|\nabla\phi_0|,\ W|_{(t=0)}=\sqrt{G(\rho_0)+A}.\end{cases} \tag{3.16}$$

The transformed system still follows the energy dissipation law. By taking the sum of the L^2 inner products of (3.7) of $\boldsymbol{u}$, of (3.9) with μ_ϕ, of (3.10) with $-\phi_t$, of (3.11) with μ_ρ, of (3.12) with $-\rho_t$, of (3.13) with $\frac{1}{2\epsilon}U$, of (3.14) with αV, of (3.15) with $2\beta W$, using the integration by parts, we then obtain the energy dissipation law of the new system (3.7)-(3.15) as

$$\frac{d}{dt}\boldsymbol{E}_{tot}(\boldsymbol{u},\phi,\rho,U,V,W)=-\nu\|\nabla\boldsymbol{u}\|^2-M_1\|\nabla\mu_\phi\|^2-M_2\|\nabla\mu_\rho\|^2\le 0. \tag{3.17}$$

In the following, we focus on designing numerical schemes for time stepping of the transformed system (3.7)-(3.15), that are linear and satisfy discrete analogues of the energy law (3.17). We fix some notations here. Let $\delta t>0$ denote the time step size and set $t_n=n\delta t$ for $0\le n\le N$ with the ending time $T=N\delta t$. We define three Sololev spaces $H^1_{per}(\Omega)=\{\phi\in H^1(\Omega):\phi\ is\ periodic\}$, $\bar{H}^1(\Omega)=\{\phi\in H^1_{per}(\Omega):\int_\Omega\phi d\boldsymbol{x}=0\}$, $H^1_{\boldsymbol{u}}(\Omega)=\{\boldsymbol{u}\in[H^1_{per}(\Omega)]^d\}$.

3.1. BDF2 scheme. We first construct a second order time stepping scheme to solve the system (3.7)-(3.15), based on the Adam-Bashforth backward differentiation formulas (BDF2).

Assuming that $(\boldsymbol{u},\phi,\rho,U,V,W)^{n-1}$ and $(\boldsymbol{u},\phi,\rho,U,V,W)^n$ are known:

step 1: we update $(\tilde{\boldsymbol{u}},\phi,\rho,U,V,W)^{n+1}$ as follows,

$$\frac{3\tilde{\boldsymbol{u}}^{n+1}-4\boldsymbol{u}^n+\boldsymbol{u}^{n-1}}{2\delta t}+B(\boldsymbol{u}^\star,\tilde{\boldsymbol{u}}^{n+1})-\nu\Delta\tilde{\boldsymbol{u}}^{n+1}+\nabla p^n+\phi^\star\nabla\mu_\phi^{n+1}+\rho^\star\nabla\mu_\rho^{n+1}=0, \tag{3.18}$$
$$\frac{3\phi^{n+1}-4\phi^n+\phi^{n-1}}{2\delta t}+\nabla\cdot(\tilde{\boldsymbol{u}}^{n+1}\phi^\star)=M_1\Delta\mu_\phi^{n+1}, \tag{3.19}$$
$$\mu_\phi^{n+1}=-\epsilon\Delta\phi^{n+1}+\frac{1}{\epsilon}\phi^\star U^{n+1}+\alpha\nabla\cdot(V^{n+1}\boldsymbol{Z}^\star), \tag{3.20}$$
$$\frac{3\rho^{n+1}-4\rho^n+\rho^{n-1}}{2\delta t}+\nabla\cdot(\tilde{\boldsymbol{u}}^{n+1}\rho^\star)=M_2\Delta\mu_\rho^{n+1}, \tag{3.21}$$
$$\mu_\rho^{n+1}=-\eta\Delta\rho^{n+1}+\alpha V^{n+1}+\beta H^\star W^{n+1}, \tag{3.22}$$

$$3U^{n+1}-4U^n+U^{n-1}=2\phi^\star(3\phi^{n+1}-4\phi^n+\phi^{n-1}), \tag{3.23}$$
$$3V^{n+1}-4V^n+V^{n-1}=(3\rho^{n+1}-4\rho^n+\rho^{n-1})-\boldsymbol{Z}^\star\cdot\nabla(3\phi^{n+1}-4\phi^n+\phi^{n-1}), \tag{3.24}$$
$$3W^{n+1}-4W^n+W^{n-1}=\frac{1}{2}H^\star(3\rho^{n+1}-4\rho^n+\rho^{n-1}), \tag{3.25}$$

with periodic boundary condition being imposed, where

$$\begin{aligned}&B(\boldsymbol{u},\boldsymbol{v})=(\boldsymbol{u}\cdot\nabla)\boldsymbol{v}+\frac{1}{2}(\nabla\cdot\boldsymbol{u})\nabla\boldsymbol{v},\\&\boldsymbol{u}^\star=2\boldsymbol{u}^n-\boldsymbol{u}^{n-1},\phi^\star=2\phi^n-\phi^{n-1},\rho^\star=2\rho^n-\rho^{n-1},\\&\boldsymbol{Z}^\star=\boldsymbol{Z}(\phi^\star),H^\star=H(\rho^\star).\end{aligned} \tag{3.26}$$

step 2: we update p^{n+1} as follows,

$$\frac{3}{2\delta t}(\boldsymbol{u}^{n+1}-\tilde{\boldsymbol{u}}^{n+1})+\nabla(p^{n+1}-p^n)=0, \tag{3.27}$$
$$\nabla\cdot\boldsymbol{u}^{n+1}=0, \tag{3.28}$$

with periodic boundary conditions.

REMARK 3.1. A pressure-correction scheme is used to decouple the computation of the pressure from that of the velocity. For the Navier-Stokes equations, there exists a large quantity of literature concerning the subjects about theoretical/numerical analysis, scheme development, as well as their applications in various research fields, see [3,6,10–12,16,19,22,30–35,40,41,44–47,49–53,58,62].

REMARK 3.2. Note that the scheme (3.18)-(3.25) is purely linear, and the computations of the variables $(\phi,\ \mu_\phi,\ \rho,\ \mu_\rho,\ \tilde{\boldsymbol{u}})^{n+1}$ are decoupled from the pressure p^{n+1} by combining the second order pressure correction scheme with a subtle implicit-explicit treatment for the stress and convective terms. We are not clear how to develop second order, energy stable schemes that can decouple the computations of all variables. Indeed, it is still an open problem on how to decouple the phase field variable from the velocity field $\boldsymbol{u}$ while preserving the unconditional energy stability and second order temporal accuracy. So far, the best, decoupled-type energy stable schemes with provable energy stabilities are just first order accurate in time (cf. [28,37–39]).

REMARK 3.3. The adopted projection method here was analyzed in [14] where it is shown (discrete time, continuous space) that the scheme is second order accurate for the velocity in $\ell^2(0,T;L^2(\Omega))$ but only first order accurate for the pressure in $\ell^\infty(0,T;L^2(\Omega))$ due to the artificial homogenous Neumann boundary condition imposed on the pressure. Since we use the periodic boundary conditions for all variables, the order of accuracy of the pressure can be second order accurate, that is shown by the numerical tests in Section 4.

Note that the new variables U, V and W will not bring up extra computational cost through the following procedure. We rewrite the Equations (3.23)–(3.25) as follows,

$$U^{n+1}=A_1+2\phi^\star\phi^{n+1}, \tag{3.29}$$
$$V^{n+1}=B_1+\rho^{n+1}-\boldsymbol{Z}^\star\cdot\nabla\phi^{n+1}, \tag{3.30}$$
$$W^{n+1}=C_1+\frac{1}{2}H^\star\rho^{n+1}, \tag{3.31}$$

where $A_1=U^{n\dagger}-2\phi^\star\phi^{n\dagger}$, $B_1=V^{n\dagger}-\rho^\dagger+\boldsymbol{Z}^\star\cdot\nabla\phi^{n\dagger}$, $C_1=W^{n\dagger}-\frac{1}{2}H^\star\rho^{n\dagger}$, and $S^{n\dagger}=\frac{4S^n-S^{n-1}}{3}$ for any variable S.

Thus the system (3.18)-(3.25) can be rewritten as

$$\begin{aligned}
&\tilde{\boldsymbol{u}}^{n+1}+\frac{2\delta t}{3}B(\boldsymbol{u}^{\star},\tilde{\boldsymbol{u}}^{n+1})-\frac{2\delta t}{3}\nu\Delta\tilde{\boldsymbol{u}}^{n+1}+\frac{2\delta t}{3}\phi^{\star}\nabla\mu_{\phi}^{n+1}+\frac{2\delta t}{3}\rho^{\star}\nabla\mu_{\rho}^{n+1}\\
&=\boldsymbol{u}^{n\dagger}-\frac{2\delta t}{3}\nabla p^{n}, \qquad (3.32)\\
&\phi^{n+1}+\frac{2\delta t}{3}\nabla\cdot(\tilde{\boldsymbol{u}}^{n+1}\phi^{\star})-\frac{2\delta t}{3}M_1\Delta\mu_{\phi}^{n+1}=\phi^{n\dagger}, \qquad (3.33)\\
&-\mu_{\phi}^{n+1}-\epsilon\Delta\phi^{n+1}+\frac{1}{\epsilon}2\phi^{\star}\phi^{\star}\phi^{n+1}+\alpha\nabla\cdot(\rho^{n+1}\boldsymbol{Z}^{\star}-\boldsymbol{Z}^{\star}\cdot\nabla\phi^{n+1}\boldsymbol{Z}^{\star})\\
&=-\frac{1}{\epsilon}\phi^{\star}A_1-\alpha\nabla\cdot(B_1\boldsymbol{Z}^{\star}), \qquad (3.34)\\
&\rho^{n+1}+\frac{2\delta t}{3}\nabla\cdot(\tilde{\boldsymbol{u}}^{n+1}\rho^{\star})-\frac{2\delta t}{3}M_2\Delta\mu_{\rho}^{n+1}=\rho^{n\dagger}, \qquad (3.35)\\
&-\mu_{\rho}^{n+1}-\eta\Delta\rho^{n+1}+\alpha\rho^{n+1}-\alpha\boldsymbol{Z}^{\star}\cdot\nabla\phi^{n+1}+\frac{1}{2}\beta H^{\star}H^{\star}\rho^{n+1}=-\alpha B_1-\beta H^{\star}C_1. \qquad (3.36)
\end{aligned}$$

Therefore, the practical implementation for solving the scheme (3.18)-(3.28) is solving the above system to obtain $(\tilde{\boldsymbol{u}},\phi,\rho)^{n+1}$, and then update $(U,V,W)^{n+1}$ through (3.29).

Now we study the well-posedness of the corresponding weak form of the semi-discretized system (3.32)-(3.36).

We define

$$\begin{aligned}
\bar{\phi}&=\frac{1}{|\Omega|}\int_{\Omega}\phi d\boldsymbol{x}, \qquad \bar{\rho}=\frac{1}{|\Omega|}\int_{\Omega}\rho d\boldsymbol{x},\\
\bar{\mu}_{\phi}&=\frac{1}{|\Omega|}\int_{\Omega}\mu_{\phi}d\boldsymbol{x}, \quad \bar{\mu}_{\rho}=\frac{1}{|\Omega|}\int_{\Omega}\mu_{\rho}d\boldsymbol{x}.
\end{aligned} \qquad (3.37)$$

By integrating (3.19) and (3.21), we obtain

$$\bar{\phi}^{n+1}=\bar{\phi}^{n}=\cdots=\bar{\phi}^{0}, \quad \bar{\rho}^{n+1}=\bar{\rho}^{n}=\cdots=\bar{\rho}^{0}. \qquad (3.38)$$

We let

$$\begin{aligned}
\phi&=\phi^{n+1}-\bar{\phi}^{0},\mu_{\phi}=\mu_{\phi}^{n+1}-\bar{\mu}_{\phi}^{0},\\
\rho&=\rho^{n+1}-\bar{\rho}^{0},\mu_{\rho}=\mu_{\rho}^{n+1}-\bar{\mu}_{\rho}^{0},
\end{aligned}$$

thus $\phi,\rho,\mu_{\phi},\mu_{\rho}\in\bar{H}^1(\Omega)$. The weak form for (3.32)-(3.36) can be written as the following system with unknowns ϕ, ρ, μ_{ϕ}, $\mu_{\rho}\in\bar{H}^1(\Omega)$, $\boldsymbol{u}\in H^1_{\boldsymbol{u}}(\Omega)$,

$$\begin{aligned}
&(\boldsymbol{u},\boldsymbol{v})+\frac{2\delta t}{3}(B(\boldsymbol{u}^{\star},\boldsymbol{u}),\boldsymbol{v})+\frac{2\delta t}{3}\nu(\nabla\boldsymbol{u},\nabla\boldsymbol{v})+\frac{2\delta t}{3}(\phi^{\star}\nabla\mu_{\phi}+\frac{2\delta t}{3}\rho^{\star}\nabla\mu_{\rho},\boldsymbol{v})\\
&=(\boldsymbol{f}_1,\boldsymbol{v}), \qquad (3.39)\\
&(\phi,w)-\frac{2\delta t}{3}(\boldsymbol{u}\phi^{\star},\nabla w)+\frac{2\delta t}{3}M_1(\nabla\mu,\nabla w)=(f_2,w), \qquad (3.40)\\
&(-\mu_{\phi},\psi)+\epsilon(\nabla\phi,\nabla\psi)+\frac{1}{\epsilon}2(\phi^{\star}\phi,\phi^{\star}\psi)-\alpha(\rho\boldsymbol{Z}^{\star},\nabla\psi)+\alpha(\boldsymbol{Z}^{\star}\cdot\nabla\phi,\boldsymbol{Z}^{\star}\cdot\nabla\psi)\\
&=(f_3,\psi), \qquad (3.41)\\
&(\rho,\varpi)-\frac{2\delta t}{3}(\boldsymbol{u}\rho^{\star},\nabla\varpi)+\frac{2\delta t}{3}M_2(\nabla\mu_{\rho},\nabla\varpi)=(f_4,\varpi), \qquad (3.42)\\
&(-\mu_{\rho},\varrho)+\eta(\nabla\rho,\nabla\varrho)+\alpha(\rho,\varrho)-\alpha(\boldsymbol{Z}^{\star}\cdot\nabla\phi,\varrho)+\frac{1}{2}\beta(H^{\star}\rho,H^{\star}\varrho)=(f_5,\varrho), \qquad (3.43)
\end{aligned}$$

for any $\boldsymbol{v}\in H^1_{\boldsymbol{u}}(\Omega)$ and $w,\psi,\varpi,\varrho\in\bar{H}^1(\Omega)$, where $\boldsymbol{f}_1$ and $f_{i,i=2,\cdots,5}$ are the corresponding terms on the right-hand side of (3.32)-(3.36).

We denote the above linear system (3.39)-(3.43) as

$$(\mathbb{L}(\boldsymbol{X}),\boldsymbol{Y})=(\mathbb{B},\boldsymbol{Y}) \tag{3.44}$$

where $\mathbb{L}$ is the linear operator, $\boldsymbol{X}=(\boldsymbol{u},\ \mu_\phi,\ \phi,\ \mu_\rho,\ \rho)^T$, and $\boldsymbol{Y}=(\boldsymbol{v},\ w,\ \psi,\ \varpi,\ \varrho)^T$, and $\boldsymbol{X},\ \boldsymbol{Y}\in(H^1_{\boldsymbol{u}},\ \bar{H}^1,\ \bar{H}^1,\ \bar{H}^1,\ \bar{H}^1)(\Omega)$.

THEOREM 3.1. *The linear system (3.44) admits a unique solution* $\boldsymbol{X}=(\boldsymbol{u},\mu_\phi,\phi,\mu_\rho,\rho)^T\in(H^1_{\boldsymbol{u}},\ \bar{H}^1,\ \bar{H}^1,\ \bar{H}^1,\ \bar{H}^1)(\Omega)$.

Proof. (i). For any $\boldsymbol{X}=(\boldsymbol{u},\mu_\phi,\phi,\mu_\rho,\rho)^T$ and $\boldsymbol{Y}=(\boldsymbol{v},w,\psi,\varpi,\varrho)^T$ with $\boldsymbol{X},\boldsymbol{Y}\in(H^1_{\boldsymbol{u}},\ \bar{H}^1,\ \bar{H}^1,\ \bar{H}^1,\ \bar{H}^1)(\Omega)$, we have

$$\begin{aligned}(\mathbb{L}(\boldsymbol{X}),\boldsymbol{Y})\le C_1(&\|\boldsymbol{u}\|_{H^1}+\|\mu_\phi\|_{H^1}+\|\phi\|_{H^1}+\|\mu_\rho\|_{H^1}+\|\rho\|_{H^1})\\ &(\|\boldsymbol{v}\|_{H^1}+\|w\|_{H^1}+\|\psi\|_{H^1}+\|\varpi\|_{H^1}+\|\varrho\|_{H^1}),\end{aligned} \tag{3.45}$$

where C_1 is a constant that depends on $\delta t,\nu,M_1,M_2,\epsilon,\alpha,\beta,\eta$, $\|\phi^\star\|_{L^\infty}$, $\|\boldsymbol{Z}^\star\|_{L^\infty}$, $\|\rho^\star\|_{L^\infty}$, and $\|H^\star\|_{L^\infty}$.

(ii). It is easy to derive that

$$\begin{aligned}(\mathbb{L}(\boldsymbol{X}),\boldsymbol{X})=&\|\boldsymbol{u}\|^2+\frac{2\delta t}{3}\nu\|\nabla\boldsymbol{u}\|^2+\frac{2\delta t}{3}M_1\|\nabla\mu_\phi\|^2+\frac{2\delta t}{3}M_2\|\nabla\mu_\rho\|^2\\ &+\epsilon\|\nabla\phi\|^2+\eta\|\nabla\rho\|^2+\frac{2}{\epsilon}\|\phi^\star\phi\|^2+\frac{\beta}{2}\|H^\star\rho\|^2+\alpha\|\rho-\boldsymbol{Z}^\star\cdot\nabla\phi\|^2\\ \ge& C_2(\|\boldsymbol{u}\|^2_{H^1}+\|\phi\|^2_{H^1}+\|\rho\|^2_{H^1}+\|\mu_\phi\|^2_{H^1}+\|\mu_\rho\|^2_{H^1}),\end{aligned} \tag{3.46}$$

where C_2 is a constant that depends on $\delta t,\nu,M_1,M_2,\epsilon,\eta$.

Then from the Lax-Milgram theorem, we conclude that the linear system (3.44) admits a unique solution $\boldsymbol{X}=(\boldsymbol{u},\mu_\phi,\phi,\mu_\rho,\rho)^T\in(H^1_{\boldsymbol{u}},\ \bar{H}^1,\ \bar{H}^1,\ \bar{H}^1,\ \bar{H}^1)(\Omega)$. ∎

The stability result of the BDF2 scheme follows along the same lines as the derivation of the new PDE energy dissipation law (3.17), as follows.

THEOREM 3.2. *The second order BDF2 scheme (3.18)-(3.28) is unconditionally energy stable, i.e., it satisfies the following discrete energy dissipation law:*

$$\frac{1}{\delta t}(E^{n+1,n}_{2nd}-E^{n,n-1}_{2nd})\le-\nu\|\nabla\tilde{\boldsymbol{u}}^{n+1}\|^2-M_1\|\nabla\mu^{n+1}_\phi\|^2-M_2\|\nabla\mu^{n+1}_\rho\|^2, \tag{3.47}$$

where

$$\begin{aligned}E^{n+1,n}_{2nd}=&\frac{1}{2}\Big(\frac{1}{2}\|\boldsymbol{u}^{n+1}\|^2+\frac{1}{2}\|2\boldsymbol{u}^{n+1}-\boldsymbol{u}^n\|^2\Big)+\frac{\delta t^2}{3}\|\nabla p^{n+1}\|^2\\ &+\frac{\epsilon}{2}\Big(\frac{1}{2}\|\nabla\phi^{n+1}\|^2+\frac{1}{2}\|2\nabla\phi^{n+1}-\nabla\phi^n\|^2\Big)+\frac{\eta}{2}\Big(\frac{1}{2}\|\nabla\rho^{n+1}\|^2+\frac{1}{2}\|2\nabla\rho^{n+1}-\nabla\rho^n\|^2\Big)\\ &+\frac{1}{4\epsilon}\Big(\frac{1}{2}\|U^{n+1}\|^2+\frac{1}{2}\|2U^{n+1}-U^n\|^2\Big)+\frac{\alpha}{2}\Big(\frac{1}{2}\|V^{n+1}\|^2+\frac{1}{2}\|2V^{n+1}-V^n\|^2\Big)\\ &+\beta\Big(\frac{1}{2}\|W^{n+1}\|^2+\frac{1}{2}\|2W^{n+1}-W^n\|^2\Big).\end{aligned} \tag{3.48}$$

Proof. By taking the L^2 inner product of (3.18) with $2\delta t\tilde{\boldsymbol{u}}^{n+1}$, we obtain

$$(3\tilde{\boldsymbol{u}}^{n+1}-4\boldsymbol{u}^n+\boldsymbol{u}^{n-1},\tilde{\boldsymbol{u}}^{n+1})+2\nu\delta t\|\nabla\tilde{\boldsymbol{u}}^{n+1}\|^2+2\delta t(\nabla p^n,\tilde{\boldsymbol{u}}^{n+1})$$

$$+2\delta t(\phi^\star\nabla\mu_\phi^{n+1},\tilde{\boldsymbol{u}}^{n+1})+2\delta t(\rho^\star\nabla\mu_\rho^{n+1},\tilde{\boldsymbol{u}}^{n+1})=0. \tag{3.49}$$

From (3.27), for any function $\boldsymbol{v}$ with $\nabla\cdot\boldsymbol{v}=0$, we can derive

$$(\boldsymbol{u}^{n+1},\boldsymbol{v})=(\tilde{\boldsymbol{u}}^{n+1},\boldsymbol{v}). \tag{3.50}$$

Then for the first term in (3.49), we have

$$\begin{aligned}
&(3\tilde{\boldsymbol{u}}^{n+1}-4\boldsymbol{u}^n+\boldsymbol{u}^{n-1},\tilde{\boldsymbol{u}}^{n+1})\\
=&(3\tilde{\boldsymbol{u}}^{n+1}-4\boldsymbol{u}^n+\boldsymbol{u}^{n-1},\boldsymbol{u}^{n+1})+(3\tilde{\boldsymbol{u}}^{n+1}-4\boldsymbol{u}^n+\boldsymbol{u}^{n-1},\tilde{\boldsymbol{u}}^{n+1}-\boldsymbol{u}^{n+1})\\
=&(3\boldsymbol{u}^{n+1}-4\boldsymbol{u}^n+\boldsymbol{u}^{n-1},\boldsymbol{u}^{n+1})+(3\tilde{\boldsymbol{u}}^{n+1},\tilde{\boldsymbol{u}}^{n+1}-\boldsymbol{u}^{n+1})\\
=&(3\boldsymbol{u}^{n+1}-4\boldsymbol{u}^n+\boldsymbol{u}^{n-1},\boldsymbol{u}^{n+1})+3(\tilde{\boldsymbol{u}}^{n+1}-\boldsymbol{u}^{n+1},\tilde{\boldsymbol{u}}^{n+1}+\boldsymbol{u}^{n+1})\\
=&\frac{1}{2}\Big(\|\boldsymbol{u}^{n+1}\|^2-\|\boldsymbol{u}^n\|^2+\|2\boldsymbol{u}^{n+1}-\boldsymbol{u}^n\|^2-\|2\boldsymbol{u}^n-\boldsymbol{u}^{n-1}\|^2\\
&+\|\boldsymbol{u}^{n+1}-2\boldsymbol{u}^n+\boldsymbol{u}^{n-1}\|^2\Big)+3(\|\tilde{\boldsymbol{u}}^{n+1}\|^2-\|\boldsymbol{u}^{n+1}\|^2),
\end{aligned} \tag{3.51}$$

where we have used the following identity

$$2(3a-4b+c,a)=|a|^2-|b|^2+|2a-b|^2-|2b-c|^2+|a-2b+c|^2. \tag{3.52}$$

For the projection step, we rewrite (3.27) as

$$\frac{3}{2\delta t}\boldsymbol{u}^{n+1}+\nabla p^{n+1}=\frac{3}{2\delta t}\tilde{\boldsymbol{u}}^{n+1}+\nabla p^n. \tag{3.53}$$

By squaring both sides of the above equality, we obtain

$$\frac{9}{4\delta t^2}\|\boldsymbol{u}^{n+1}\|^2+\|\nabla p^{n+1}\|^2=\frac{9}{4\delta t^2}\|\tilde{\boldsymbol{u}}^{n+1}\|^2+\|\nabla p^n\|^2+\frac{3}{\delta t}(\tilde{\boldsymbol{u}}^{n+1},\nabla p^n), \tag{3.54}$$

namely, by multiplying $2\delta t^2/3$, we have

$$\frac{3}{2}(\|\boldsymbol{u}^{n+1}\|^2-\|\tilde{\boldsymbol{u}}^{n+1}\|^2)+\frac{2\delta t^2}{3}(\|\nabla p^{n+1}\|^2-\|\nabla p^n\|^2)=2\delta t(\tilde{\boldsymbol{u}}^{n+1},\nabla p^n). \tag{3.55}$$

By taking the L^2 inner product of (3.27) with $2\delta t\boldsymbol{u}^{n+1}$, we have

$$\frac{3}{2}(\|\boldsymbol{u}^{n+1}\|^2-\|\tilde{\boldsymbol{u}}^{n+1}\|^2+\|\boldsymbol{u}^{n+1}-\tilde{\boldsymbol{u}}^{n+1}\|^2)=0. \tag{3.56}$$

By combining (3.49), (3.51), (3.55), and (3.56), we obtain

$$\begin{aligned}
&\frac{1}{2}(\|\boldsymbol{u}^{n+1}\|^2-\|\boldsymbol{u}^n\|^2+\|2\boldsymbol{u}^{n+1}-\boldsymbol{u}^n\|^2-\|2\boldsymbol{u}^n-\boldsymbol{u}^{n-1}\|^2+\|\boldsymbol{u}^{n+1}-2\boldsymbol{u}^n+\boldsymbol{u}^{n-1}\|^2)\\
&+\frac{3}{2}\|\boldsymbol{u}^{n+1}-\tilde{\boldsymbol{u}}^{n+1}\|^2+\frac{2\delta t^2}{3}(\|\nabla p^{n+1}\|^2-\|\nabla p^n\|^2)+2\nu\delta t\|\nabla\tilde{\boldsymbol{u}}^{n+1}\|^2\\
&+2\delta t(\phi^\star\nabla\mu_\phi^{n+1},\tilde{\boldsymbol{u}}^{n+1})+2\delta t(\rho^\star\nabla\mu_\rho^{n+1},\tilde{\boldsymbol{u}}^{n+1})=0.
\end{aligned} \tag{3.57}$$

By taking the L^2 inner product of (3.19) with $2\delta t\mu_\phi^{n+1}$, we obtain

$$(3\phi^{n+1}-4\phi^n+\phi^{n-1},\mu_\phi^{n+1})-2\delta t(\phi^\star\tilde{\boldsymbol{u}}^{n+1},\nabla\mu_\phi^{n+1})=-2M_1\delta t\|\nabla\mu_\phi^{n+1}\|^2. \tag{3.58}$$

By taking the L^2 inner product of (3.20) with $-(3\phi^{n+1}-4\phi^n+\phi^{n-1})$ and applying (3.52), we obtain

$$\begin{aligned}
&-(\mu_\phi^{n+1},3\phi^{n+1}-4\phi^n+\phi^{n-1})\\
&=-\frac{\epsilon}{2}\Big(\|\nabla\phi^{n+1}\|^2-\|\nabla\phi^n\|^2+\|2\nabla\phi^{n+1}-\nabla\phi^n\|^2-\|2\nabla\phi^n-\nabla\phi^{n-1}\|^2\\
&\quad+\|\nabla\phi^{n+1}-2\nabla\phi^n+\nabla\phi^{n-1}\|^2\Big)-\frac{1}{\epsilon}(\phi^\star U^{n+1},3\phi^{n+1}-4\phi^n+\phi^{n-1})\\
&\quad+\alpha(V^{n+1}\boldsymbol{Z}^\star,\nabla(3\phi^{n+1}-4\phi^n+\phi^{n-1})).
\end{aligned}\tag{3.59}$$

By taking the L^2 inner product of (3.21) with $2\delta t\mu_\rho^{n+1}$, we obtain

$$(3\rho^{n+1}-4\rho^n+\rho^{n-1},\mu_\rho^{n+1})-2\delta t(\rho^\star\tilde{\boldsymbol{u}}^{n+1},\nabla\mu_\rho^{n+1})=-2M_2\delta t\|\nabla\mu_\rho^{n+1}\|^2.\tag{3.60}$$

By taking the L^2 inner product of (3.22) with $-(3\rho^{n+1}-4\rho^n+\rho^{n-1})$, we obtain

$$\begin{aligned}
&-(\mu_\rho^{n+1},3\rho^{n+1}-4\rho^n+\rho^{n-1})\\
&=-\frac{\eta}{2}\Big(\|\nabla\rho^{n+1}\|^2-\|\nabla\rho^n\|^2+\|2\nabla\rho^{n+1}-\nabla\rho^n\|^2-\|2\nabla\rho^n-\nabla\rho^{n-1}\|^2\\
&\quad+\|\nabla\rho^{n+1}-2\nabla\rho^n+\nabla\rho^{n-1}\|^2\Big)-\alpha(V^{n+1},3\rho^{n+1}-4\rho^n+\rho^{n-1})\\
&\quad-\beta(H^\star W^{n+1},3\rho^{n+1}-4\rho^n+\rho^{n-1}).
\end{aligned}\tag{3.61}$$

By taking the L^2 inner product of (3.23) with $\frac{1}{2\epsilon}U^{n+1}$, we obtain

$$\begin{aligned}
&\frac{1}{4\epsilon}\Big(\|U^{n+1}\|^2-\|U^n\|^2+\|2U^{n+1}-U^n\|^2-\|2U^n-U^{n-1}\|^2+\|U^{n+1}-2U^n+U^{n-1}\|^2\Big)\\
&=\frac{1}{\epsilon}(\phi^\star(3\phi^{n+1}-4\phi^n+\phi^{n-1}),U^{n+1}).
\end{aligned}\tag{3.62}$$

By taking the L^2 inner product of (3.24) with αV^{n+1}, we obtain

$$\begin{aligned}
&\frac{\alpha}{2}(\|V^{n+1}\|^2-\|V^n\|^2+\|2V^{n+1}-V^n\|^2-\|2V^n-V^{n-1}\|^2+\|V^{n+1}-2V^n+V^{n-1}\|^2)\\
&=\alpha(3\rho^{n+1}-4\rho^n+\rho^{n-1},V^{n+1})-\alpha(\boldsymbol{Z}^\star\nabla(3\phi^{n+1}-4\phi^n+\phi^{n-1}),V^{n+1}).
\end{aligned}\tag{3.63}$$

By taking the L^2 inner product of (3.25) with $2\beta W^{n+1}$, we obtain

$$\begin{aligned}
&\beta(\|W^{n+1}\|^2-\|W^n\|^2+\|2W^{n+1}-W^n\|^2-\|2W^n-W^{n-1}\|^2\\
&\quad+\|W^{n+1}-2W^n+W^{n-1}\|^2)=\beta(H^\star(3\rho^{n+1}-4\rho^n+\rho^{n-1}),W^{n+1}).
\end{aligned}\tag{3.64}$$

Combination of (3.57), (3.58)–(3.64) gives us

$$\begin{aligned}
&\frac{1}{2}(\|\boldsymbol{u}^{n+1}\|^2-\|\boldsymbol{u}^n\|^2+\|2\boldsymbol{u}^{n+1}-\boldsymbol{u}^n\|^2-\|2\boldsymbol{u}^n-\boldsymbol{u}^{n-1}\|^2+\|\boldsymbol{u}^{n+1}-2\boldsymbol{u}^n+\boldsymbol{u}^{n-1}\|^2)\\
&+\frac{3}{2}\|\boldsymbol{u}^{n+1}-\tilde{\boldsymbol{u}}^{n+1}\|^2+\frac{2\delta t^2}{3}(\|\nabla p^{n+1}\|^2-\|\nabla p^n\|^2)\\
&+\frac{\epsilon}{2}\Big(\|\nabla\phi^{n+1}\|^2-\|\nabla\phi^n\|^2+\|2\nabla\phi^{n+1}-\nabla\phi^n\|^2-\|2\nabla\phi^n-\nabla\phi^{n-1}\|^2\\
&+\|\nabla\phi^{n+1}-2\nabla\phi^n+\nabla\phi^{n-1}\|^2\Big)\\
&+\frac{\eta}{2}\Big(\|\nabla\rho^{n+1}\|^2-\|\nabla\rho^n\|^2+\|2\nabla\rho^{n+1}-\nabla\rho^n\|^2-\|2\nabla\rho^n-\nabla\rho^{n-1}\|^2\\
&+\|\nabla\rho^{n+1}-2\nabla\rho^n+\nabla\rho^{n-1}\|^2\Big)
\end{aligned}$$

$$
\begin{aligned}
&+\frac{1}{4\epsilon}\Big(\|U^{n+1}\|^2-\|U^n\|^2+\|2U^{n+1}-U^n\|^2-\|2U^n-U^{n-1}\|^2+\|U^{n+1}-2U^n+U^{n-1}\|^2\Big)\\
&+\frac{\alpha}{2}\Big(\|V^{n+1}\|^2-\|V^n\|^2+\|2V^{n+1}-V^n\|^2-\|2V^n-V^{n-1}\|^2+\|V^{n+1}-2V^n+V^{n-1}\|^2\Big)\\
&+\beta\Big(\|W^{n+1}\|^2-\|W^n\|^2+\|2W^{n+1}-W^n\|^2-\|2W^n-W^{n-1}\|^2\\
&+\|W^{n+1}-2W^n+W^{n-1}\|^2\Big)\\
=&-2\nu\delta t\|\nabla\tilde{\boldsymbol{u}}^{n+1}\|^2-2M_1\delta t\|\nabla\mu_\phi^{n+1}\|^2-2M_2\delta t\|\nabla\mu_\rho^{n+1}\|^2.
\end{aligned}
$$

Finally, we obtain the result (3.47) after dropping some positive terms from the above equation. ∎

3.2. Crank-Nicolson scheme. One also can easily develop an alternative version of second order scheme based on the Crank-Nicolson-type scheme. It reads as follows.

Assuming that $(\boldsymbol{u},\phi,\rho,U,V,W)^{n-1}$ and $(\boldsymbol{u},\phi,\rho,U,V,W)^n$ are known,

step 1: we update $\tilde{\boldsymbol{u}}^{n+1}$, ϕ^{n+1}, ρ^{n+1}, U^{n+1}, V^{n+1}, W^{n+1} from

$$\frac{\tilde{\boldsymbol{u}}^{n+1}-\boldsymbol{u}^n}{\delta t}+B(\boldsymbol{u}^\flat,\tilde{\boldsymbol{u}}^{n+\frac12})-\nu\Delta\tilde{\boldsymbol{u}}^{n+\frac12}+\nabla p^n+\phi^\flat\nabla\mu_\phi^{n+\frac12}+\rho^\flat\nabla\mu_\rho^{n+\frac12}=0, \tag{3.65}$$

$$\frac{\phi^{n+1}-\phi^n}{\delta t}+\nabla\cdot(\tilde{\boldsymbol{u}}^{n+\frac12}\phi^\flat)=M_1\Delta\mu_\phi^{n+\frac12}, \tag{3.66}$$

$$\mu_\phi^{n+\frac12}=-\epsilon\Delta\phi^{n+\frac12}+\frac{1}{\epsilon}\phi^\flat U^{n+\frac12}+\alpha\nabla\cdot(V^{n+\frac12}\boldsymbol{Z}^\flat), \tag{3.67}$$

$$\frac{\rho^{n+1}-\rho^n}{\delta t}+\nabla\cdot(\rho^\flat\tilde{\boldsymbol{u}}^{n+\frac12})=M_2\Delta\mu_\rho^{n+\frac12}, \tag{3.68}$$

$$\mu_\rho^{n+\frac12}=-\eta\Delta\rho^{n+\frac12}+\alpha V^{n+\frac12}+\beta H^\flat W^{n+\frac12}, \tag{3.69}$$

$$U^{n+1}-U^n=2\phi^\flat(\phi^{n+1}-\phi^n), \tag{3.70}$$

$$V^{n+1}-V^n=(\rho^{n+1}-\rho^n)-\boldsymbol{Z}^\flat\cdot\nabla(\phi^{n+1}-\phi^n), \tag{3.71}$$

$$W^{n+1}-W^n=\frac12 H^\flat(\rho^{n+1}-\rho^n), \tag{3.72}$$

with periodic boundary condition being imposed, where

$$
\begin{aligned}
&\tilde{\boldsymbol{u}}^{n+\frac12}=\frac{\tilde{\boldsymbol{u}}^{n+1}+\boldsymbol{u}^n}{2},\\
&\phi^{n+\frac12}=\frac{\phi^{n+1}+\phi^n}{2},\rho^{n+\frac12}=\frac{\rho^{n+1}+\rho^n}{2},\\
&U^{n+\frac12}=\frac{U^{n+1}+U^n}{2},V^{n+\frac12}=\frac{V^{n+1}+V^n}{2},W^{n+\frac12}=\frac{W^{n+1}+W^n}{2},\\
&\phi^\flat=\frac32\phi^n-\frac12\phi^{n-1},\rho^\flat=\frac32\rho^n-\frac12\rho^{n-1},\boldsymbol{u}^\flat=\frac32\boldsymbol{u}^n-\frac12\boldsymbol{u}^{n-1},\\
&\boldsymbol{Z}^\flat=\boldsymbol{Z}(\frac32\phi^n-\frac12\phi^{n-1}),H^\flat=H(\frac32\rho^n-\frac12\rho^{n-1}).
\end{aligned}
\tag{3.73}
$$

.

step 2: we update $\boldsymbol{u}^{n+1}$ and p^{n+1} from

$$\frac{1}{\delta t}(\boldsymbol{u}^{n+1}-\tilde{\boldsymbol{u}}^{n+1})+\frac12(\nabla p^{n+1}-\nabla p^n)=0, \tag{3.74}$$

$$\nabla\cdot\boldsymbol{u}^{n+1}=0, \tag{3.75}$$

with the periodic boundary conditions.

The well-posedness and unconditional energy stability of the Crank-Nicolson scheme can be easily proved in the similar way of handling the BDF2 scheme. Therefore we just present the energy stability theorem and leave the detailed proofs to the interested readers.

THEOREM 3.3. *The second order Crank-Nicolson scheme (3.65)–(3.75) is unconditionally energy stable, i.e., it satisfies the following discrete energy dissipation law:*

$$\frac{1}{\delta t}(E_{2nd-cn}^{n+1,n}-E_{2nd-cn}^{n,n-1})\leq-\nu\|\nabla\tilde{\boldsymbol{u}}^{n+1}\|^2-M_1\|\nabla\mu_\phi^{n+\frac{1}{2}}\|^2-M_2\|\nabla\mu_\rho^{n+\frac{1}{2}}\|^2, \quad (3.76)$$

where

$$E_{2nd-cn}^{n+1,n}=\frac{1}{2}\|\boldsymbol{u}^{n+1}\|^2+\frac{\delta t^2}{8}\|\nabla p^{n+1}\|^2 +\frac{\epsilon}{2}\|\nabla\phi^{n+1}\|^2+\frac{\eta}{2}\|\nabla\rho^{n+1}\|^2+\frac{1}{4\epsilon}\|U^{n+1}\|^2+\frac{\alpha}{2}\|V^{n+1}\|^2+\beta\|W^{n+1}\|^2. \quad (3.77)$$

4. Numerical examples

We now present numerical experiments in two and three dimensions to validate the theoretical results derived in the previous section and demonstrate the efficiency, energy stability and accuracy of the proposed numerical schemes. In all examples, we set the domain $\Omega=[0,2\pi]^d, d=2,3$. If not explicitly specified, the default values of order parameters are given as follows,

$$\widehat{\epsilon}=1\times10^{-4}, M_\mu=M_\rho=1\times10^{-2}, \epsilon=5\times10^{-2}, \alpha=1\times10^{-2}, \beta=5\times10^{-2}, \nu=1, A=1 \quad (4.1)$$

We use the Fourier-spectral method to discretize the space, and 129^d Fourier modes are used so that the errors from the spatial discretization are negligible compared to the time discretization errors.

4.1. Accuracy test. We first test convergence rates of proposed BDF2 scheme (3.18)-(3.28). The following initial conditions

$$\begin{cases}\phi_0(x,y)=0.1\cos(3x)+0.4\cos(y),\\ \rho_0(x,y)=0.2\sin(2x)+0.5\sin(y)\end{cases} \quad (4.2)$$

are used. We perform the refinement test of the time step size. Since the exact solutions are not known, we choose the approximate solution obtained by using the scheme with a tiny time step size $\delta t=1.5625\times10^{-4}$ as the benchmark solution for computing errors. We present the L^2 errors of all variables between the numerical solutions and the benchmark solution at $t=0.2$ with different time step sizes in Figure 4.1. We observe that the scheme is almost perfect second order accurate in time.

4.2. Coarsening effect of two circles. In this example, we test the scheme BDF2 by using the initial conditions of two circles with different radii to see how the coarsening effects execute. We set the initial condition as

$$\begin{cases}\phi_0(x,y)=\sum_{i=1}^{2}-\tanh(\frac{\sqrt{(x-x_i)^2+(y-y_i)^2}-r_i}{1.2\epsilon})+1,\\ \rho_0(x,y)=0.3,\end{cases} \quad (4.3)$$

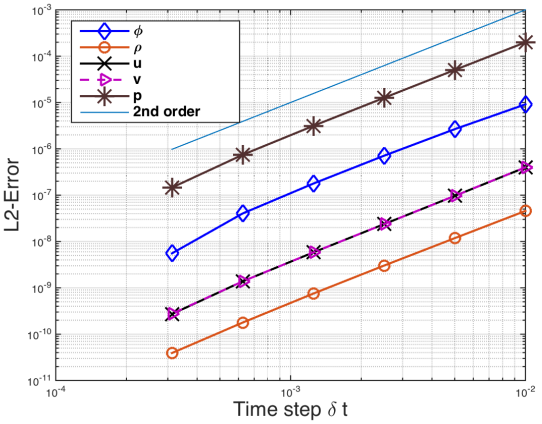

FIG. 4.1. *The L^2 numerical errors of all variables $\phi,\rho,\boldsymbol{u}=(u,v),p$ at $t=0.2$ that are computed using the scheme BDF2 and various temporal resolutions with the initial conditions of (4.2) for mesh refinement test in time.*

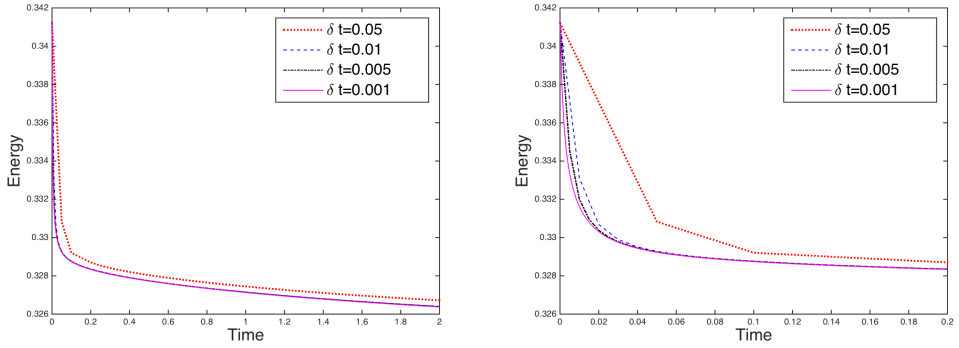

FIG. 4.2. *Time evolution of the free energy functional (3.48) for four different time step sizes, $\delta t=5\times10^{-2}$, 1×10^{-2}, 5×10^{-3}, and 1×10^{-3} for the Example 4.2 with default parameters (4.1). The energy curves show the decays for all time step sizes, that confirms that our algorithm is unconditionally stable. The left subfigure is the energy profile for $t\in[0,2]$, and the right subfigure is a close-up view for $t\in[0,0.2]$.*

where $(x_1,y_1,r_1)=(\pi-0.7,\pi-0.6,1.5)$ and $(x_2,y_2,r_2)=(\pi+1.65,\pi+1.6,0.7)$.

We emphasize that any time step size δt is allowable for the computations from the stability concern since all developed schemes are unconditionally energy stable. But larger time step will definitely induce large numerical errors. Therefore, we need to discover the rough range of the allowable maximum time step size in order to obtain good accuracy and to have as low computational cost as possible. This time step range could be estimated through the energy evolution curve plots, shown in Figure 4.2, where we compare the time evolution of the discrete free energy (3.48) for four different time step sizes until $t=2$ using the scheme BDF2. We observe that all four energy curves decay monotonically, which numerically confirms that our algorithms are unconditionally energy stable. For smaller time steps of $\delta t=1\times10^{-3}$, 5×10^{-2} and 1×10^{-2}, the three energy curves coincide very well. But for the largest time step of

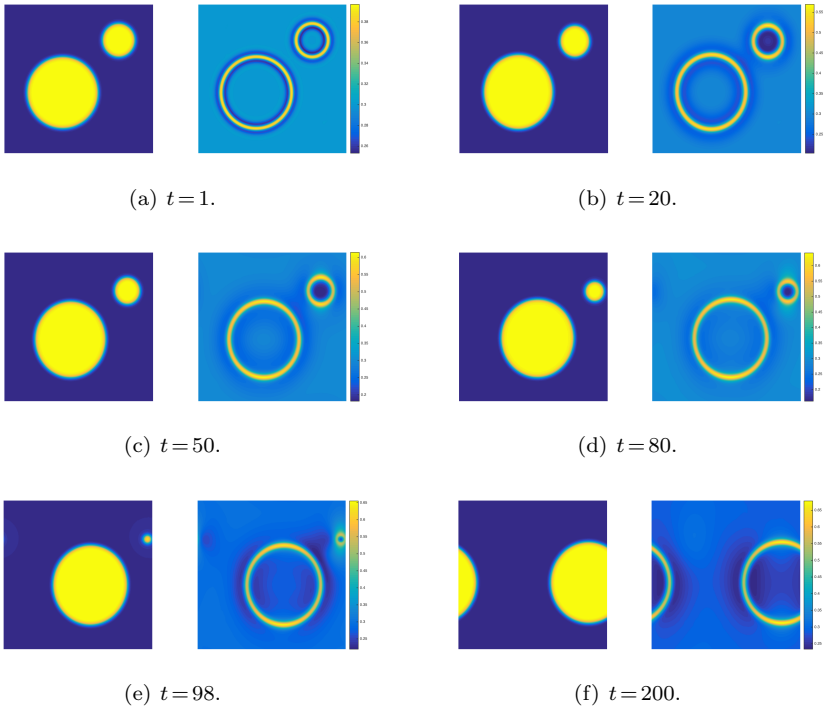

(a) $t=1$. (b) $t=20$.

(c) $t=50$. (d) $t=80$.

(e) $t=98$. (f) $t=200$.

FIG. 4.3. *Snapshots of the phase variables ϕ and ρ are taken at $t=1,20,50,80,98,200$ for Example 4.2 by using the initial condition (4.3). For each panel, the left subfigure is the profile of ϕ and the right subfigure is the profile of ρ.*

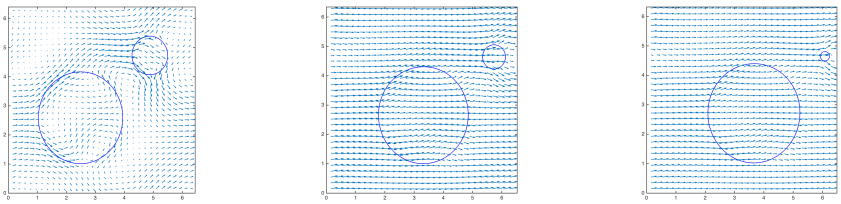

(a) $t=20$. (b) $t=80$. (c) $t=98$.

FIG. 4.4. *Profiles of the velocity field $\boldsymbol{u}$ together with the interface contour $\{\phi=0\}$ for Example 4.2 by using the initial condition (4.3). Snapshots are taken at $t=20$, 80, 98.*

$\delta t=5\times10^{-2}$, the energy curve deviates viewably away from others. This means the adopted time step size should not be larger than 5×10^{-2}, in order to get reasonably good accuracy.

In Figure 4.3, we show the evolutions of the phase field variable ϕ and concentration variable ρ at various times by using the time step $\delta t=1\times10^{-3}$. We observe the coarsening effect that the small circle is absorbed into the big circle, and the total absorption happens at around $t=98$. The velocity field $\boldsymbol{u}$, together with the interface contours of ϕ, are plotted in Figure 4.4. The time evolutions of the two free energy functionals, the modified free energy (3.48) (in terms of the three new variables) and the original

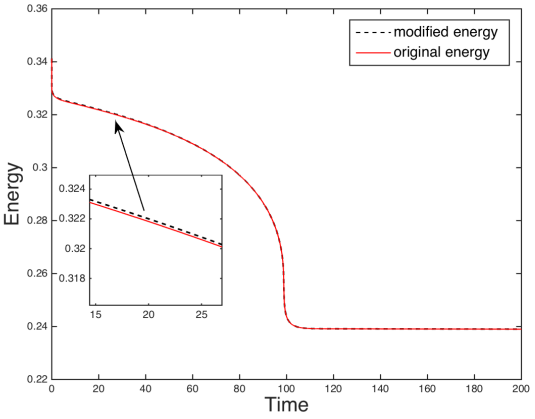

FIG. 4.5. *Time evolution of the two free energy functionals for the Example 4.2, the modified energy (3.48) and the original energy (3.2), by using the initial condition (4.3). The small inset figure is a close-up view.*

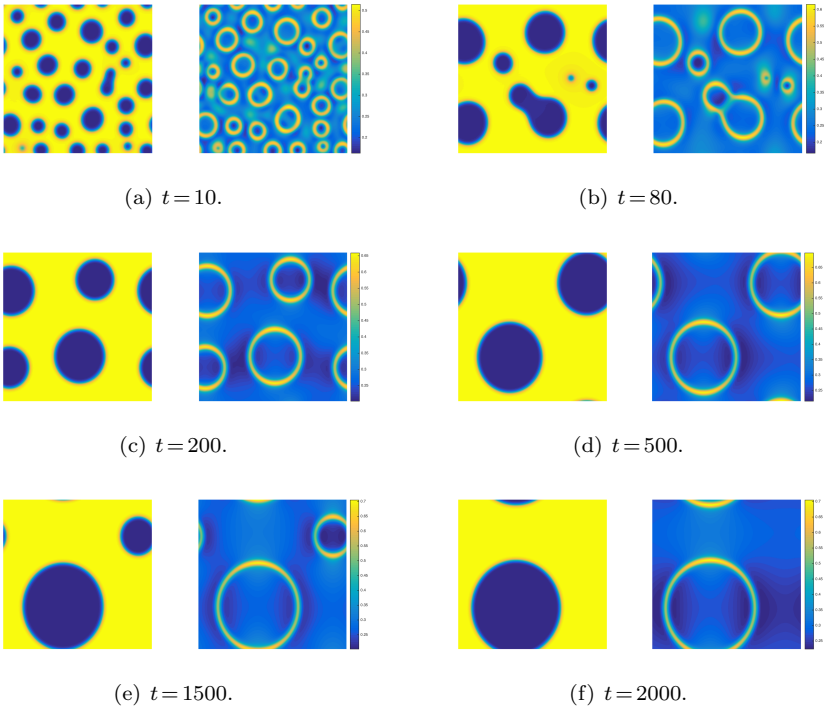

(a) $t=10$. (b) $t=80$.

(c) $t=200$. (d) $t=500$.

(e) $t=1500$. (f) $t=2000$.

FIG. 4.6. *2D spinodal decomposition for random initial data of (4.4). Snapshots of phase variables ϕ and ρ are taken at $t=10$, 80, 200, 500, 1500 and 2000. For each panel, the left subfigure is the profile of ϕ, and the right subfigure is the profile of ρ.*

energy (3.2), are plotted in Figure 4.5. It is remarkable that these two energies actually coincide very well, and both of them decay to the equilibrium, monotonically. At around $t=100$, the energies undergo a rapid decrease when the small circle is compeletly

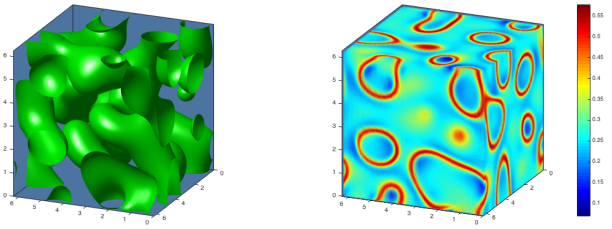

(a) $t=5$.

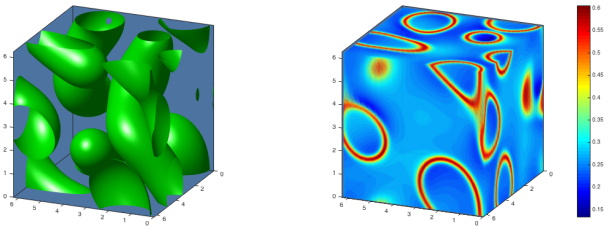

(b) $t=15$.

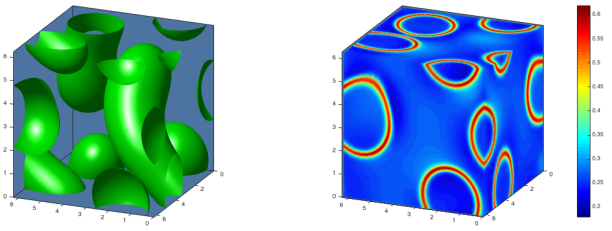

(c) $t=25$.

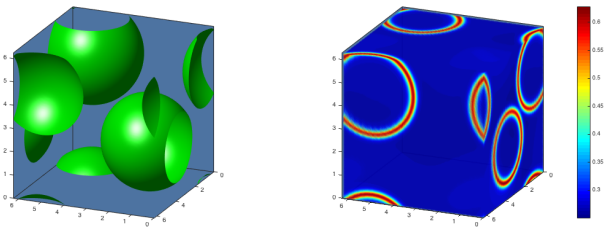

(d) $t=95$.

FIG. 4.7. *3D spinodal decomposition for random initial data of* (4.5). *Snapshots of phase variables* ϕ *and* ρ *are taken at* $t=5$, 15, 25, *and* 95. *For each panel, the left subfigure is the profile of* ϕ *(isosurfaces of* $\{\phi=0\}$*), and the right subfigure is the profile of* ρ *(that is visualized by 128 cross-sections along the z-axis).*

absorbed. Soon after that, the system achieves the equilibrium of circular shape.

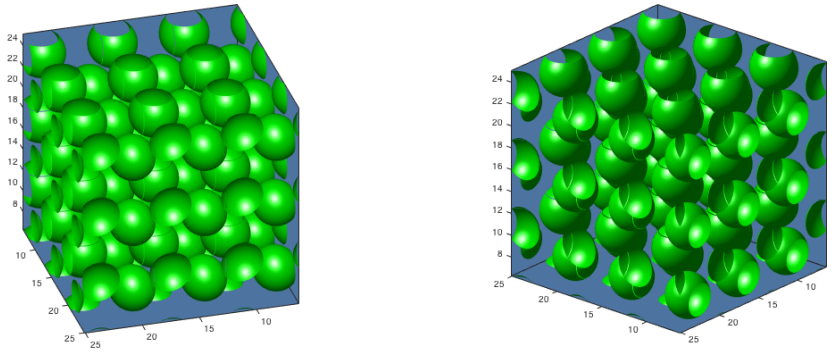

FIG. 4.8. *The isosurfaces* $\{\phi=0\}$ *of the steady state solution at* $t=95$ *of the 3D spinodal decomposition example for* 4 *periods, i.e.,* $[0,8\pi]^3$. *The two subfigures are from different angles of view.*

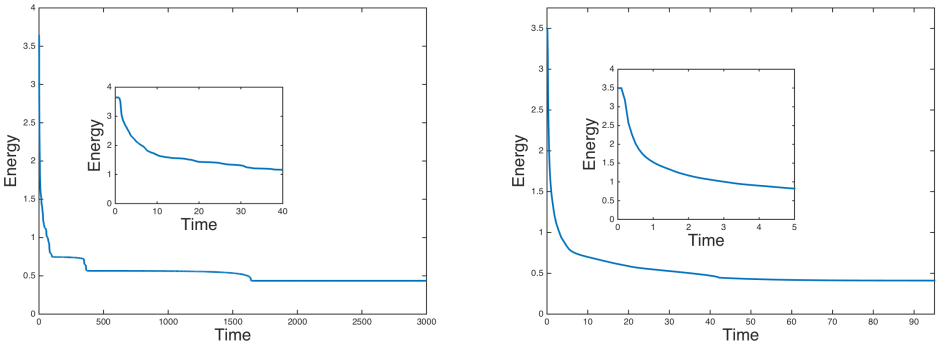

FIG. 4.9. *(From left to right:) Time evolution of the free energy functional* (3.48) *of the 2D and 3D spinodal decompositions, respectively. The small inset figure is a close-up showing where the energy decreases fast.*

4.3. Spinodal decomposition in 2D and 3D. In this example, we study the phase separation behaviors in the 2D and 3D spaces that are called spinodal decomposition. The process of the phase separation can be studied by considering a homogeneous binary mixture, which is quenched into the unstable part of its miscibility gap. In this case, the spinodal decomposition takes place, which manifests in the spontaneous growth of the concentration fluctuations that leads the system from the homogeneous to the two-phase state. Shortly after the phase separation starts, the domains of the binary components are formed and the interface between the two phases can be specified.

The initial conditions are taken as randomly perturbed fields. For 2D, it reads as

$$\phi_0(x,y)=0.4+0.001\text{rand}(x,y),\ \rho_0(x,y)=0.3; \tag{4.4}$$

and for 3D, it reads as

$$\phi_0(x,y,z)=0.4+0.001\text{rand}(x,y,z),\ \rho_0(x,y)=0.3, \tag{4.5}$$

where the rand$(\cdot)$ is the random number in $[-1,1]$ and has zero mean.

We choose the time step size $\delta t=1\times10^{-3}$ to perform both the 2D and 3D simulations. In Figure 4.6, we show the snapshots of ϕ and ρ for the 2D simulations, where

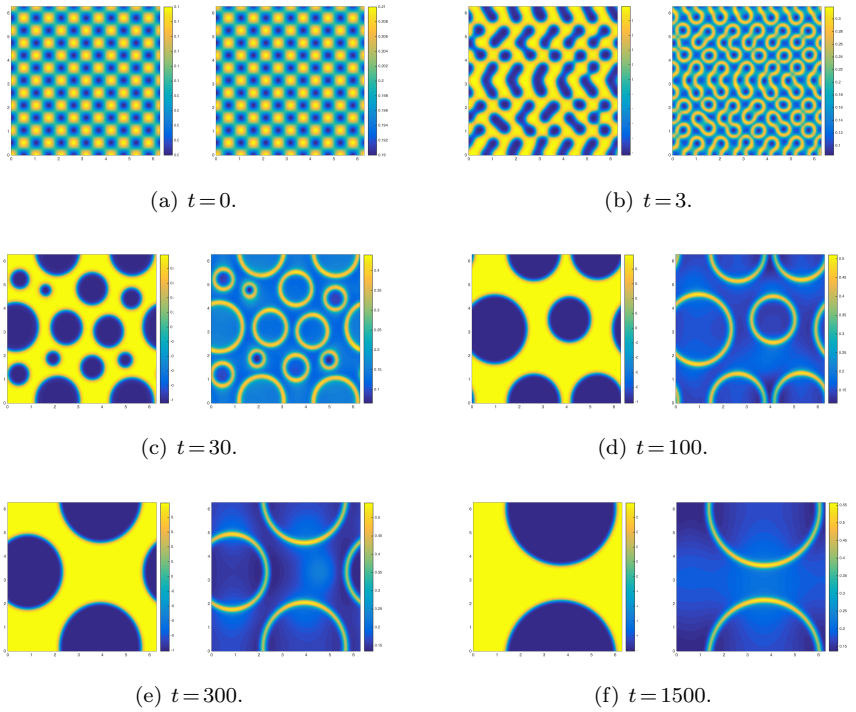

(a) $t=0$. (b) $t=3$.

(c) $t=30$. (d) $t=100$.

(e) $t=300$. (f) $t=1500$.

FIG. 4.10. *Snapshots of the phase variables ϕ and ρ are taken at $t=0$, 3, 30, 100, 300, and 1500 for Example 4.4.2, where the surfactants are distributed uniformly initially. For each panel, the left subfigure is the profile of ϕ and the right subfigure is the profile of ρ.*

we observe the coarsening dynamics that the fluid component with the less volume accumulates to small satellite drops everywhere. When the time evolves, the small drops will collide, merge and form drops with bigger sizes. The final equilibrium solution is obtained around after $t=1700$, where all small bubbles accumulate into a big bubble.

In Figure 4.7, we show the snapshots of ϕ and ρ for the 3D simulations. Similar to the 2D case, the two fluids initially are well mixed, and they soon start to decompose and accumulate. The final steady state (shown in Figure 4.7(d)) is consistent with the 2D results, namely, all small bubbles accumulate to form the final big bubble. In order to obtain a more accurate view, since the computed domain is periodic, in Figure 4.8, we plot the isosurface for 4 periods, i.e., $[0,8\pi]^3$. In Figure 4.9, we present the evolution of the total free energy (3.48) for both these simulations, that clearly shows that the energies always monotonically decay with respect to the time.

4.4. Surfactant absorption.

4.4.1. Surfactant uniformly distributed initially. We assume the fluid interface and the surfactant are uniformly distributed over the domain initially and the specific profiles (shown in Figure 4.10 (a)) are chosen

$$\phi_0(x,y)=0.1+0.01\cos(6x)\cos(6y), \tag{4.6}$$

$$\rho_0(x,y)=0.2+0.01\cos(6x)\cos(6y). \tag{4.7}$$

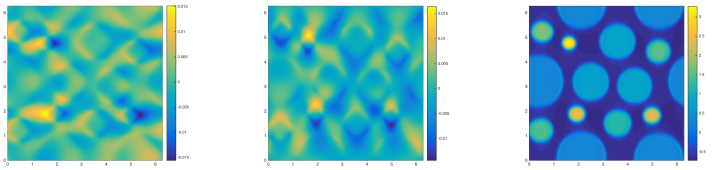

(a) The first component of the velocity field $\boldsymbol{u}=(u,v)$ at $t=30,300,1500$.

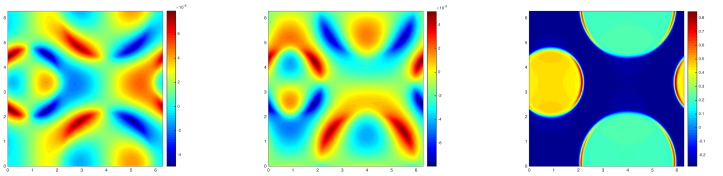

(b) The second component of the velocity field $\boldsymbol{u}=(u,v)$ at $t=30,300,1500$.

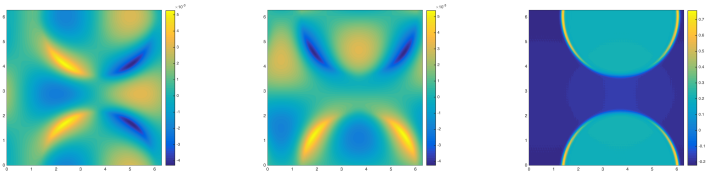

(c) The pressure p at $t=30,300,1500$.

FIG. 4.11. *Profiles of the velocity field* $\boldsymbol{u}=(u,v)$ *and the pressure* p. *Snapshots are taken at* $t=30$, 300 *and* 1500 *for the Example 4.4.1.*

We take the time step size $\delta t=1\times10^{-3}$. Figure 4.10 shows the snapshots of coarsening dynamics at $t=0,3,30,100,300,1500$ and the final steady shape forms a big drop. Driven by the coupling entropy energy term, the surfactant is absorbed into the binary fluid interfaces so that the higher concentration appears near the interfaces than other regions. In Figure 4.11, we show the profiles of the velocity $\boldsymbol{u}$ and p at $t=30$, 300 and 1500.

4.4.2. Surfactant locally distributed initially. In this example, we assume the fluid interface and the surfactant field are mismatched over the domain initially. The specific initial profiles (shown as Figure 4.12 (a)) are chosen as

$$\phi_0(x,y)=0.1+0.01\cos(6x)\cos(6y), \tag{4.8}$$

$$\rho_0(x,y)=0.8\exp\Big(-\frac{(x-\pi)^2+(y-\pi)^2}{1.25^2}\Big). \tag{4.9}$$

When $t=0$, the phase field variable ϕ is same as the previous example, but the surfactant concentration variable ϕ is locally accumulated around the center of the domain. We still take the time step size $\delta t=1\times10^{-3}$ for better accuracy. Figure 4.12 shows the snapshots of the dynamics behaviors of ϕ and ρ at various times. We observe that, since the surfactant is initially concentrated at the center, it takes longer times for the surfactant to diffuse away from this center region. Consequently, during the early stage of the evolution, the higher concentration of surfactant only appears around the center

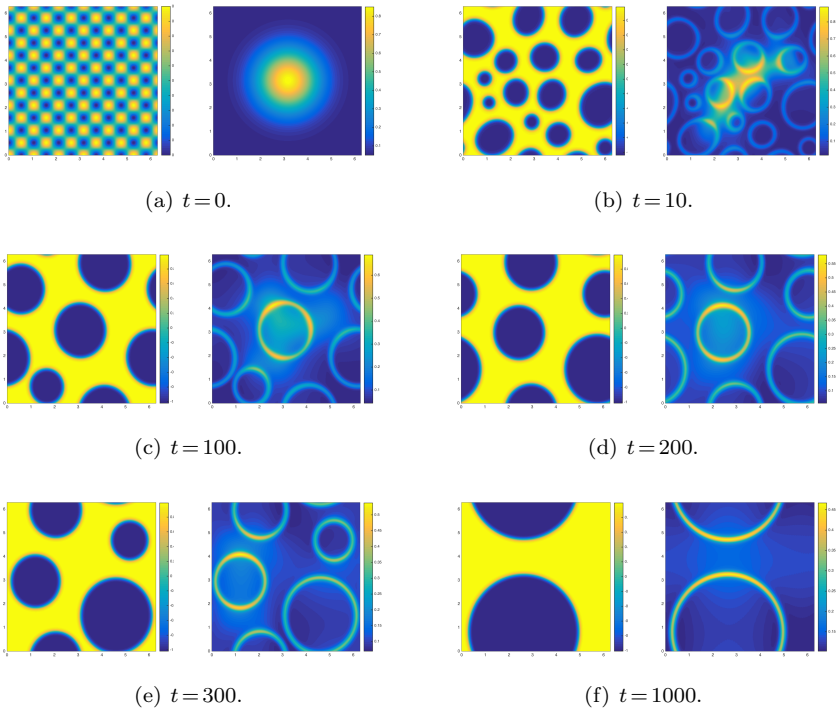

(a) $t=0$. (b) $t=10$.

(c) $t=100$. (d) $t=200$.

(e) $t=300$. (f) $t=1000$.

FIG. 4.12. *Snapshots of the phase variables ϕ and ρ are taken at $t=0$, 10, 100, 200, 300, and 1000 for Example 4.4.2, where the surfactants are initially distributed in a center circle. For each panel, the left subfigure is the profile of ϕ and the right subfigure is the profile of ρ.*

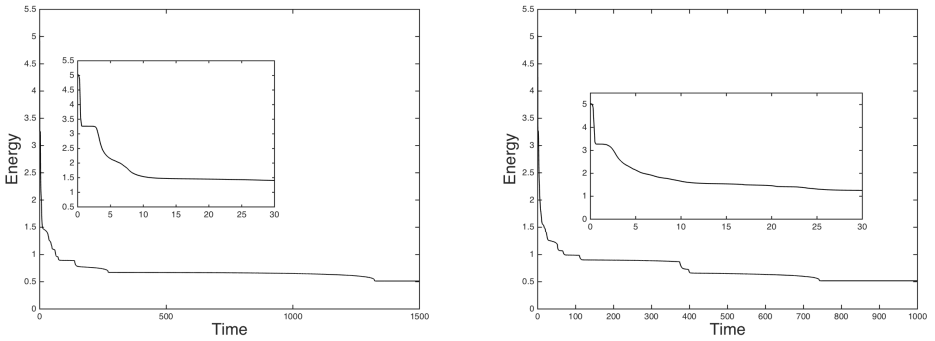

FIG. 4.13. *Time evolution of the free energy functional (3.6) for the Examples 4.4.1 and 4.4.2, respectively. The small inset figure is a close-up view showing where the energy decreases fast.*

area of the domain. The surfactant completely diffuses and is absorbed into the binary fluid interfaces after around $t=300$. We finally plot the evolution of energy curves in Figure 4.13 for the Example 4.4.1 and the Example 4.4.2, respectively. Overall, the numerical solutions of both the examples present similar features to those obtained in [13, 42].

5. Concluding remarks

In this paper, two efficient schemes are developed for solving the hydrodynamics coupled binary fluid-surfactant phase field model. The scheme is designed by combining the second order pressure correction method, the newly developed IEQ approach, and implicit-explicit treatments for the stress and convective terms. The obtained schemes are purely linear and second-order accurate in time. We rigorously prove that the induced linear systems are well-posed and the schemes are unconditionally energy stable. Finally, various 2D and 3D numerical examples are presented to validate the accuracy and stability of the proposed scheme.

Acknowledgments. C. Xu is partially supported by NSFC-61872429. C. Chen is partially supported by the NSFC-11771375 and NSFC-11571297, Shandong Province Natural Science Foundation ZR2018MAQ008. X. Yang is partially supported by NSF DMS-1720212 and DMS-1818783. X. He is partially supported by the National Science Foundation under grant number DMS-1722647.

REFERENCES

[1] D. M. Anderson, G. B. McFadden, and A. A. Wheeler, *Diffuse-interface methods in fluid mechanics*, Annu. Rev. Fluid Mech., 30:139–165, 1998. 2

[2] J. Bueno and H. Gomez, *Liquid-vapor transformations with surfactants. phase-field model and isogeometric analysis*, J. Comput. Phys., 321(part A):797–818, 2016. 1

[3] C. Chen, X. He, and J. Huang, *Mechanical quadrature methods and their extrapolations for solving the first kind boundary integral equations of Stokes equation*, Appl. Num. Math., 96:165–179, 2015. 3.1

[4] L. Chen, J. Zhao, and X. Yang, *Regularized linear schemes for the molecular beam epitaxy model with slope selection*, Appl. Num. Math., 128:139–156, 2018. 3

[5] M. I. M. Copetti and C. M. Elliott, *Numerical analysis of the Cahn-Hilliard equation with a logarithmic free energy*, Numer. Math., 63(4):39–65, 1992. 3, 3

[6] R. Duan and Z. Xiang, *A note on global existence for the chemotaxis-Stokes model with nonlinear diffusion*, Int. Math. Res. Notices, 7:1833–1852, 2014. 3.1

[7] C. M.Elliott and H. Garcke, *On the Cahn-Hilliard equation with degenerate mobility*, SIAM J. Math. Anal., 27:404–423, 1996. 3, 3

[8] S. Engblom, M. Do-Quang, G. Amberg, and A.-K. Tornberg, *On diffuse interface modeling and simulation of surfactants in two-phase fluid flow*, Comput. Phys. Comm., 14:879–915, 2013. 2.1

[9] I. Fonseca, M. Morini, and V. Slastikov, *Surfactants in foam stability: A phase-field model*, Arch. Rational Mech. Anal., 183:411–456, 2007. 1, 2

[10] Y. Gao, X. He, L. Mei, and X. Yang, *Fully decoupled, linearized, and energy stable finite element method for Cahn-Hilliard-Navier-Stokes-Darcy model*, SIAM. J. Sci. Comput., 40:B110–B137, 2018. 3, 3.1

[11] Z. Ge, M. Feng, and Y. He, *A stabilized nonconfirming finite element method based on multiscale enrichment for the stationary Navier-Stokes equations*, Appl. Math. Comput., 202:700–707, 2008. 3.1

[12] Z. Ge, M. Feng, and Y. He, *Stabilized multiscale finite element method for the stationary Navier-Stokes equations*, J. Mech. Anal. Appl., 354:708–717, 2009. 3.1

[13] S. Gu, H. Zhang, and Z. Zhang, *An energy-stable finite-difference scheme for the binary fluid-surfactant system*, J. Comput. Phys., 270:416–431, 2014. 1, 4.4.2

[14] J. L. Guermond, *Un résultat de convergence d'ordre deux en temps pour l'approximation des équations de Navier-Stokes par une technique de projection incrémentale*, M2AN Math. Model. Numer. Anal., 33:169–189, 1999. 3.3

[15] J. L. Guermond, P. Minev, and J. Shen, *An overview of projection methods for incompressible flows*, Comput. Meth. Appl. Mech. Engrg., 195:6011–6045, 2006. 3

[16] J. L. Guermond, J. Shen, and X. Yang, *Error analysis of fully discrete velocity-correction methods for incompressible flows*, Math. Comp., 77:1387–1405, 2008. 3.1

[17] M. E. Gurtin, D. Polignone, and J. Viñals, *Two-phase binary fluids and immiscible fluids described by an order parameter*, Math. Models Meth. Appl. Sci., 6(6):815–831, 1996. 2

[18] D. Han, A. Brylev, X. Yang, and Z. Tan, *Numerical analysis of second order, fully discrete energy*

stable schemes for phase field models of two phase incompressible flows, J. Sci. Comput., 70:965–989, 2016. 3

[19] Z.-J. Hu, T.-Z. Huang, and N.-B. Tan, *A splitting preconditioner for the incompressible Navier-Stokes equations*, Math. Modelling and Anal., 18:612–630, 2013. 3.1

[20] Q. Huang, X. Yang, and X. He, *Numerical approximations for a smectic–a liquid crystal flow model: First-order, linear, decoupled and energy stable schemes*, Discrete Contin. Dyn. Syst.-B, 23:2177–2192, 2018. 3

[21] D. Jacqmin, *Calculation of two-phase Navier-Stokes flows using phase-field modeling*, J. Comput. Phys., 155(1):96–127, 1999. 2

[22] S. Jiang and Y. Ou, *Incompressible limit of the non-isentropic Navier-Stokes equations with well-prepared initial data in three-dimensional bounded domains*, J. Math. Pures Appl., 96:1–28, 2011. 3.1

[23] J. Kim, *Numerical simulations of phase separation dynamics in a water-oil-surfactant system*, J. Colloid Interface Sci., 303:272–279, 2006. 1

[24] S. Komura and H. Kodama, *Two-order-parameter model for an oil-water-surfactant system*, Phys. Rev. E., 55:1722–1727, 1997. 1, 2.1

[25] M. Laradji, H. Guo, M. Grant, and M. J. Zuckermann, *The effect of surfactants on the dynamics of phase separation*, J. Phys. Condens. Matter, 4(32):6715–6728, 1992. 1, 2.1

[26] M. Laradji, O. G. Mouristen, S. Toxvaerd, and M. J. Zuckermann, *Molecular dynamics simulations of phase separation in the presence of surfactants*, Phys. Rev. E., 50:1243–1252, 1994. 1, 2.1

[27] C. Liu and J. Shen, *A phase field model for the mixture of two incompressible fluids and its approximation by a Fourier-spectral method*, Phys. D, 179(3-4):211–228, 2003. 2

[28] S. Minjeaud, *An unconditionally stable uncoupled scheme for a triphasic Cahn-Hilliard/ Navier-Stokes model*, Commun. Comput. Phys., 29:584–618, 2013. 3.2

[29] L. Onsager, *Reciprocal relations in irreversible processes. II*, Phys. Rev., 38:2265, 1931. 2

[30] Y. Ou, *Low Mach number limit of viscous polytropic fluid flows*, J. Diff. Eqs., 251:2037–2065, 2011. 3.1

[31] Y. Ou and D. Ren, *Incompressible limit of global strong solutions to 3-D barotropic Navier-Stokes equations with well-prepared initial data and Navier's slip boundary conditions*, J. Math. Anal. Appl., 420:1316–1336, 2014. 3.1

[32] D. Ren and Y. Ou, *Strong solutions to an Oldroyd-B model with slip boundary conditions via incompressible limit*, Math. Meth. Appl. Sci., 38:330–348, 2014. 3.1

[33] X. Ren, J. Wu, Z. Xiang, and Z. Zhang, *Global existence and decay of smooth solution for the 2-D MHD equations*, J. Funct. Anal., 267:503–541, 2014. 3.1

[34] X. Ren, Z. Xiang, and Z. Zhang, *Global existence and decay of smooth solutions for the 3-D MHD-type equations without magnetic diffusion*, Sci. China. Math., 59:1949–1974, 2016. 3.1

[35] X. Ren, Z. Xiang, and Z. Zhang, *Global well-posedness for the 2D MHD equations without magnetic diffusion in a strip domain*, Nonlinearity, 29:1257–1291, 2016. 3.1

[36] J. Shen, J. Xue, and J. Yang, *The scalar auxiliary variable (SAV) approach for gradient flows*, J. Comput. Phys., 353:407–416, 2018. 3

[37] J. Shen and X. Yang, *Decoupled energy stable schemes for phase filed models of two phase complex fluids*, SIAM J. Sci. Comput., 36:B122–B145, 2014. 3.2

[38] J. Shen and X. Yang, *Decoupled, energy stable schemes for phase-field models of two-phase incompressible flows*, SIAM J. Num. Anal., 53(1):279–296, 2015. 3.2

[39] J. Shen, X. Yang, and H. Yu, *Efficient energy stable numerical schemes for a phase field moving contact line model*, J. Comput. Phys., 284:617–630, 2015. 3.2

[40] N.-B. Tan, T.-Z. Huang, and Z.-J. Hu, *A relaxed splitting preconditioner for the incompressible Navier-Stokes equations*, J. Appl. Math., 2012:402490, 2012. 3.1

[41] N.-B. Tan, T.-Z. Huang, and Z.-J. Hu, *Incomplete augmented Lagrangian preconditioner for steady incompressible Navier-Stokes equations*, Sci. World J., 2013:486323, 2013. 3.1

[42] C. H. Teng, I. L. Chern, and M. C. Lai, *Simulating binary fluid-surfactant dynamics by a phase field model*, Discrete Contin. Dyn, Syst.-B, 17:1289–1307, 2010. 1, 2, 4.4.2

[43] R. van der Sman and S. van der Graaf, *Diffuse interface model of surfactant adsorption onto flat and droplet interfaces*, Rheol. Acta, 46:3–11, 2006. 1, 2

[44] Y. Wang, C. Mu, and Z. Xiang, *Properties of positive solution for nonlocal reaction-diffusion equation with nonlocal boundary*, Bound. Value Probl., 207:064579, 2007. 3.1

[45] Y. Wang and Z. Xiang, *Boundedness in a quasilinear 2D parabolic-parabolic attraction-repulsion chemotaxis system*, J. Korean Math. Soc., 21:1953–1973, 2016. 3.1

[46] Y. Wang and Z. Xiang, *Global existence and boundedness in a Keller-Segel-Stokes system involving a tensor-valued sensitivity with saturation: The 3D case*, J. Diff. Eqs., 261:4944–4973, 2016. 3.1

[47] Z. Wang, Z. Xiang, and P. Yu, *Asymptotic dynamics on a singular chemotaxis system modeling onset of tumor angiogenesis*, J. Diff. Eqs., 260:2225–2258, 2016. 3.1

[48] X. Wu, G. J. van Zwieten, and K. G. van der Zee, *Stabilized second-order convex splitting schemes for Cahn-Hilliard models with application to diffuse-interface tumor-growth models*, Int. J. Numer. Meth. Biomed. Engng., 30:180–203, 2014. 3

[49] Z. Xiang, *The regularity criterion of the weak solution to the 3D viscous Boussinesq equations in Besov spaces*, Appl. Math. Comput., 34:360–372, 2011. 3.1

[50] Z. Xiang, Q. Chen, and C. Mu, *Blow-up rate estimates for a system of reaction-diffusion equations with absorption*, J. Korean Math. Soc., 44:779–786, 2007. 3.1

[51] Z. Xiang, Q. Chen, and C. Mu, *Critical curves for degenerate parabolic equations coupled via non-linear boundary flux*, Appl. Math. Comput., 189:549–559, 2007. 3.1

[52] Z. Xiang, Y. Wang, and H. Yang, *Global existence and nonexistence for degenerate parabolic equations with nonlinear boundary flux*, Comput. Math. Appl., 62:3056–3065, 2011. 3.1

[53] Z. Xiang and H. Yang, *On the regularity criteria for the 3D magneto-micropolar fluids in terms of one directional derivative*, Bound. Value Probl., 2012:139, 2012. 3.1

[54] X. Yang, *Linear, first and second order and unconditionally energy stable numerical schemes for the phase field model of homopolymer blends*, J. Comput. Phys., 302:509–523, 2016. 3

[55] X. Yang and D. Han, *Linearly first- and second-order, unconditionally energy stable schemes for the phase field crystal equation*, J. Comput. Phys., 330:1116–1134, 2017. 3

[56] X. Yang and L. Ju, *Efficient linear schemes with unconditionally energy stability for the phase field elastic bending energy model*, Comput. Meth. Appl. Mech. Engrg., 315:691–712, 2017. 3

[57] X. Yang and L. Ju, *Linear and unconditionally energy stable schemes for the binary fluid-surfactant phase field model*, Comput. Meth. Appl. Mech. Engrg., 318:1005–1029, 2017. 1, 3

[58] X. Yang, G. Zhang, and X. He, *Convergence analysis of an unconditionally energy stable projection scheme for magneto-hydrodynamic equations*, Appl. Num. Math., 136:235–256, 2019. 3.1

[59] X. Yang, J. Zhao, and X. He, *Linear, second order and unconditionally energy stable schemes for the viscous Cahn-Hilliard equation with hyperbolic relaxation using the invariant energy quadratization method*, J. Comput. Appl. Math., 343:80–97, 2018. 3

[60] X. Yang, J. Zhao, and Q. Wang, *Numerical approximations for the molecular beam epitaxial growth model based on the invariant energy quadratization method*, J. Comput. Phys., 333:104–127, 2017. 3

[61] X. Yang, J. Zhao, Q. Wang, and J. Shen, *Numerical approximations for a three components Cahn-Hilliard phase-field model based on the invariant energy quadratization method*, M3AS: Math. Models Meth. Appl. Sci., 27:1993–2030, 2017. 3

[62] Y. Zhang, M. Feng, and Y. He, *Subgrid model for the stationary incompressible Navier-Stokes equations based on the high order polynomial interpolation*, Int. J. Num. Anal. Modelling, 7:734–748, 2010. 3.1

[63] J. Zhao, Q. Wang, and X. Yang, *Numerical approximations for a phase field dendritic crystal growth model based on the invariant energy quadratization approach*, Inter. J. Num. Meth. Engr., 110:279-300, 2017. 3

[64] J. Zhao, X. Yang, Y. Gong, and Q. Wang, *A novel linear second order unconditionally energy stable scheme for a hydrodynamic Q-tensor model of liquid crystals*, Comput. Meth. Appl. Mech. Engrg., 318:803-825, 2017. 3